ATTAINING DESIRED DEFORMATIONS OF FLEXIBLE STRUCTURES THROUGH MECHANICAL AND NON-MECHANICAL STIMULI

A Thesis

by

RENZHE CHEN

Submitted to the Office of Graduate and Professional Studies of
Texas A&M University
in partial fulfillment of the requirements for the degree of

MASTER OF SCIENCE

Chair of Committee,   Anastasia Muliana
Committee Members, Alan Freed
                         Negar Kalantar
Head of Department, Andreas A. Polycarpou

May 2018

Major Subject: Mechanical Engineering

ABSTRACT

The development of flexible and foldable structures is a game-changing technology in many engineering, architecture, and design fields. This technology allows for structures and devices that are reusable, adaptable, portable and deployable while performing their desired functions. One classical example is deployable antennas for space applications. Recent applications are in biomedicine, architectural facades, transformable- and portable shelters, among others. This study presents parametric studies on understanding deformations of two types of flexible structures activated by thermal and mechanical stimuli. The first type of flexible structures consists of bilayer materials, which have significant differences in their thermo-mechanical properties. The second type is made of relatively stiff flat panels with relief cutting or kerfing patterns. The kerfing patterns increase the flexibilities of the plates. Parametric studies are conducted on these flexible structures in order to examine the effects of the material and geometrical parameters on the overall deformations of the structures. Several applications are illustrated in order to show how to form the desired shapes by designing the flexible structures with certain microstructural characteristics.

CONTRIBUTORS AND FUNDING SOURCES

TABLE OF CONTENTS

LIST OF FIGURES

LIST OF TABLES

CHAPTER I

INTRODUCTION

1.1 Literature review

Flexible and lightweight structures are gaining popularity in recent engineering applications. For example, in space applications, lightweight and flexible structures can dramatically reduce the cost of deployable systems, while in automotive industries, these structures can significantly increase the efficiency of vehicles. It is becoming necessary to understand the characteristics of these flexible and foldable structures in order to design structures for various applications.

Some of flexible structures are integrated with smart materials, like thermo-electric materials, piezoelectric materials, shape memory alloys etc. so that these structures have the ability of sensing and adapting in response to the external stimuli (thermal field, electrical field, optical field and so on). Significant efforts have been made on the development of smart materials. Otsuka and Wayman found that SMPs (shape memory polymers) possessing dual-shape ability can undergo relatively large deformations under external stimuli [1], which found many applications as sensors and actuators, e.g., Liu [2], Li [3], Suo [4], etc. In order to increase the stiffness and strength of the SMPs, Gunes and Jana [5] and Meng and Hu [6] have considered adding hybrid fillers to the SMPs. It is shown that the reinforced SMP composites have better performance like easy processing, lightweight, low cost, corrosion resistance, compared to the original ones. For example Gall presented bending analysis to test two groups of samples, resin transfer molded (RTM) specimens and pre-impregnated (pre-preg) pressed samples to

1

find that such composites can recover approximately 100% back to the original states after undergoing large deformations [7], while Tendon's experiments focused on the durability of these materials exposed to harsh environmental like UV radiation, moisture and so on [8]. EAPs (electroactive polymers) are also another type of compliant materials, which have electro-mechanical coupling stimuli. The non-contact actuation characteristics makes it suitable for soft robotics applications. Bar-Cohen and Stewart [9], Samatham [10], Kornbluh [11] have shown that some EAP have the potential to mimic movements of muscles. Several analytical and numerical models have been presented in order to investigate the deformation in smart compliant systems exposed to non-mechanical stimuli. Tajeddini et al. presented a numerical study of flexible composite structures using piezoelectric actuators [12]. They investigated the effect of nonlinear electro-mechanical coupling behaviors of piezoelectric materials on the deformations of active compliant structures. Ask et al. presented a coupled electro-viscoelastic model for electrostrictive PU based on the experiment data. The model is implemented in a finite element formulation for analyzing response of electro-active structures, e.g., [13][14][15].

A number of flexible structures are often subjected to severe environmental conditions like high temperatures and/or high temperature gradients. These thermal effects will have a huge impact on the performance of these structures, and these thermal behaviors can actually be utilized to achieve certain functions and/or desired deformations. Boley and Weiner discussed basic linear theory of thermal stress in beams under thermal variation [16]. Boley also extended the elementary beam theory when considering the temperature effects on composite beams of rectangular cross section

[17]. Many researches (Horvay and Born [18], Durelli and Tsao [19]) have focused on the stress and displacement formulations under a uniform temperature change, while Eischen has presented a thermal stress analysis on a composite strip under temperature gradients [20]. Recently, there are several other approaches in incorporating the thermal effects on the deformations of composites and structures. Khan [21] and Jeon [22] both considered thermal effects in determining the overall deformations of viscoelastic materials and composites. Khan included coupled heat conduction and deformation in analyzing response of polymers and composites, due to the energy dissipation effect. It is known that the thermal stimulus can have a detrimental effect to structures, such as reduction in mechanical properties at elevated temperature or accelerated aging in materials. However, one can also utilize the thermal effect in materials and structures in order to achieve desired functions. One of the classic examples is the applications of bimetallic strips, e.g., thermostats, thermometers, circuit breakers. Due to its potential applications, there have been many analytical and numerical studies on determining the deformations in composite systems under thermal stimulus. Zhang conducted theoretical analysis combined with finite element analysis in order to determine the bistable behaviors of the anti-symmetrical composite shells under uniform temperature field and thermal gradient through the thickness [23]. Bartels et al. presented a reduced non-linear model of bilayer plates including diffusion under thermal actuation and a new finite element method was formulated for determining the 3D large deformations of the thin layer structures [24]. They showed that various folding and shape reconfigurations can be achieved by prescribing a thermal stimulus to the bilayer systems.

The most common type of flexible structures is of slender beams or plates, in which the planar dimension of these structures is much higher than their thickness, so that they have low second moment of an area with respect to the planar axes. There has been another method to create flexible structures instead of relying mainly on the slender structures. Relief cutting is one of architecture practical techniques to create a flexible planar surface from relatively stiff materials like MDF (Medium density fiberboard). The mechanisms are based on reducing the second moment of an area of the plates through several cutting patterns, in order to induce large out of plane deformations. There are a great variety of relief cutting patterns created by designers. Hoffer, taking the advantage of wooden properties, used the kerfing of wood to finish the design of a pavilion [25]. Bending of the corners is achieved due to the compliant characteristics in these regions, which were achived through kerfing.

Dujam Ivanišević first invented an interlocked Archimedean spirals pattern, which can obtain double-curvature panels [26]. Based on the 2D meander pattern, Zarrinmehr et al. used a remeshing method to provide an algorithm to obtain more general results, in which local properties of these patterns can be controlled to acquire the desired stiffness [27]. Instead of studying on design and fabrication process, Guzelci set up a basic three-step experimentation to present the affordance of the bending behavior of the planar surface [28]. Greenberg and Korner also investigated a subtractive material technique in architectural systems but he focused more on shapes found in the nature systems like biological creatures which may have great applications in architecture designs. [29].

1.2 Motivations and Research Objectives

Non- mechanical stimuli are attractive for inducing various shape changes in structures owing to its non-contact characteristics. This allows for remotely controlling the deformations in structures which find many applications in engineering field, e.g., biomedicine, aerospace structures, and architectures. Temperature is one of the widely used and controllable sources of non-mechanical stimulus. The intelligent structures can be designed this way in response to the environment temperature to achieve its configuration for certain purposes. In order to properly design thermally activated flexible and compliant structures, there is a need to understand several material and geometrical parameters that influence the deformations in such flexible and compliant structures. The ultimate goal is to be able to design flexible structures with desired deformed shapes by prescribing thermal stimulus.

Also, in architecture world, laser cutting has a great variety of applications to create fantastic flexible and compliant structures. In addition to the expression of art and beauty, they may have great potential in engineering areas. By controlling the stiffness of these structures, one can achieve many desired configurations with relatively small mechanical stimulus. Various shapes and patterns on architectural walls have a great advantage for acoustic purposes. To guide the design of flexible and compliant structures through wood cutting methods, there is a need for understanding of the mechanism of the deformations of the cut patterns. In the future, it is also possible to integrate active materials to the panels of different cut patterns so that the deformed shapes of these structures can be remotely controlled and adaptable to various environmental conditions.

The research objective of this study is to conduct parametric studies on understanding deformations in flexible structures actuated by mechanical and thermal stimuli. The first flexible system is comprised of bilayer composites which significant differences in the ratio of the thermal expansion between these two materials. An analytical solution is presented on a rather simple bilayer beam subjected to temperature changes and the result is compared to numerical solution from finite element (FE) analysis. Next, numerical simulation is performed on bilayer composite plates under a uniform temperature change. The effect of several parameters related to the geometry and material for the patches and substrates are analyzed in order to understand their effects on the overall plate deformations. Upon this understanding, a smart star-shaped plate and a saddle shape are created as examples of self-folding structures under thermal loadings.

The second flexible system is on utilizing the architecture kerfing patterns in order to generate flexible structures under mechanical loadings. Although many works have been done to make use of cuttings to create flexible structures in architecture and construction field, limited works related to the mechanics of these structures are conducted to give the full understanding of the compliant characteristics of these kerfing structures. In this work, we will carry out some analysis on the unit sections of the relief cutting pattern to present some results of the affordance of the stretching, bending and twisting behaviors. After that, we can utilize these unit sections for some practical applications. Numerical simulations using FE are used for this purpose. The effects of different cutting density and mesh size on the deformation are also studied. Uniaxial extension experiments are conducted on these different cutting density unit

cells to test their stretching behaviors. These unit-cells have great difference in flexibilities. By arranging the unit-cells with different density, various deformed configurations can be achieved.

CHAPTER II

BILAYER COMPOSITE STRUCTURES UNDER THERMAL

LOADINGS

2.1 Two-layered beam under thermal loadings

For our study on large deformation behaviors of composite beams under uniform temperature loadings, a bonded two-layered beam is considered first shown in the Figure II.1. The analytical solution obtained from the beam theory is compared to the one from finite element (FE) analysis. The purpose is to examine the validity in using an approximate solution for analyzing thermal deformations of flexible structures under more complex boundary conditions. The origin of the beam is located on the left end of the bonded surface of the beam. The x-axis and y-axis are longitudinal and wide axes, respectively, while the z axis is in the out-of-plane direction. The i-th layer is denoted by subscript i (i=1, 2) and b_i and h_i refer to the width and thickness of each layer. α_i and E_i denote the thermal expansion ratio, thermal stress and elastic modulus of each layer respectively, while T is the uniform temperature change.
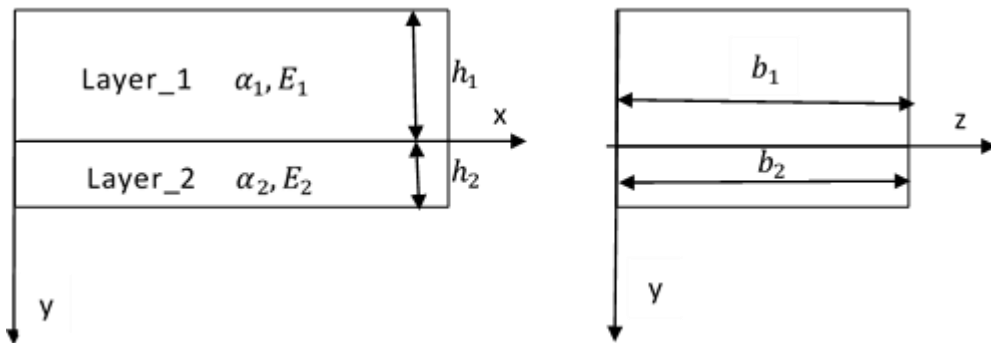
Figure II.1 Two-layered beam from two perspectives

8

The strains ϵ_{xi} after the deformation are expressed by equation (II.1)

$$\epsilon_{xi} = \alpha_i T + \frac{\sigma_{xi}}{E_i} = \epsilon_0 + \frac{y}{\rho} \quad (i = 1,2) \tag{II.1}$$

where ϵ_0 and $\frac{1}{\rho}$ denote the strain and the curvature at y=0, respectively.

Since there are no external forces applied on the beam, then

$$\int_A \sigma dA = 0 \; ; \int_A \sigma y dA = 0 \tag{II.2}$$

Due to the constant width of the beam, the equations (II.2) can be simplified by

$$\int_{-h_1}^{0} \sigma_{x1} b_1 dy + \int_{0}^{h_2} \sigma_{x2} b_2 dy = 0 \tag{II.3}$$

$$\int_{-h_1}^{0} \sigma_{x1} b_1 y dy + \int_{0}^{h_2} \sigma_{x2} b_2 y dy = 0 \tag{II.4}$$

Combining the equation (II.3) and (II.4) to eliminate σ_{xi}, we can get

$$2(E_2 h_2 b_2 + E_1 h_1 b_1)\epsilon_0 + (E_2 h_2^2 b_2 - E_1 h_1^2 b_1)\frac{1}{\rho}$$
$$= 2\int_{-h_1}^{0} \alpha_1 E_1 T_1(y) b_1 dy + 2\int_{0}^{h_2} \alpha_2 E_2 T_2(y) b_2 dy \tag{II.5}$$

$$3(E_2 h_2^2 b_2 + E_1 h_1^2 b_1)\epsilon_0 + 2(E_2 h_2^3 b_2 - E_1 h_1^3 b_1)\frac{1}{\rho}$$
$$= 6\int_{-h_1}^{0} \alpha_1 E_1 T_1(y) b_1 y dy + 6\int_{0}^{h_2} \alpha_2 E_2 T_2(y) b_2 y dy \tag{II.6}$$

With the equations (II.5) and (II.6), ϵ_0 and $\frac{1}{\rho}$ can be denoted by

$$\varepsilon_0 = \frac{2}{D}\left\{ 2\left[\int_{-h_1}^{0} \alpha_1 E_1 T_1(y) b_1 dy + \int_{0}^{h_2} \alpha_2 E_2 T_2(y) b_2 dy\right](E_2 h_2^3 b_2 \right.$$
$$+ E_1 h_1^3 b_1)$$
$$- 3\left[\int_{-h_1}^{0} \alpha_1 E_1 T_1(y) b_1 dy + \int_{0}^{h_2} \alpha_2 E_2 T_2(y) b_2 dy\right](E_2 h_2^2 b_2$$
$$\left. - E_1 h_1^2 b_1)\right\} \tag{II.7}$$

$$\frac{1}{\rho} = \frac{6}{D}\left\{2\left[\int_{-h_1}^{0}\alpha_1 E_1 T_1(y)b_1 y\,dy + \int_{0}^{h_2}\alpha_2 E_2 T_2(y)b_2 y\,dy\right](E_2 h_2 b_2\right.$$
$$+ E_1 h_1 b_1)$$
$$-\left[\int_{-h_1}^{0}\alpha_1 E_1 T_1(y)b_1\,dy + \int_{0}^{h_2}\alpha_2 E_2 T_2(y)b_2\,dy\right](E_2 h_2^2 b_2 \qquad \text{(II.8)}$$
$$\left.- E_1 h_1^2 b_1)\right\}$$

where
$$D = (E_2 h_2^2 b_2 - E_1 h_1^2 b_1)^2 + 4E_1 E_2 h_1 h_2 (h_1 + h_2)^2 b_1 b_2 \qquad \text{(II.9)}$$

With equation (II.7), (II.8) and (II.9), the curvature can be determined, considered here as a parameter (C^*). We adopt the relation between the curvatures and the deflections for large displacement of an elastic beam, see Muliana [30], which gives the displacements along the longitudinal axis of the beam:

$$u_{x0} = \frac{\varepsilon_0}{C^*}\sin(C^* x) - x \qquad \text{(II.10)}$$

$$u_{y0} = \frac{\varepsilon_0}{C^*}\cos(C^* x) - \frac{\varepsilon_0}{C^*} \qquad \text{(II.11)}$$

where the u_{x0} and u_{y0} are components of the displacement in x and y directions, respectively.

In order to examine the analytical model and FE analysis for the bilayer beam under different temperature changes, we consider a specific two-layered beam case and the parameters for each layer are given in Table II.1.

Table II.1 Parameters for each layer of the beam

	Layer_1	Layer_2
Young's modulus	2.9E5 psi	7.3E6 psi
Poisson's ratio	0.2	0.38
Thermal expansion ratio	150×10^{-6}	5×10^{-6}
Length	0.79 inch	0.79 inch
Height	0.06 inch	0.04 inch

In the contrast with the analytical solutions, a 2D shell FE (Finite Element) model is created. The linear elastic shell element S4R is used in the model and the element size is 0.02 inch, after conducting a parametric study. The results of the tip deflections under different uniform temperature changes are summarized in Table II.2 and Figure II.2.

Table II.2 The relation between temperature change and displacement from analytical and numerical results

Temperature change (^{o}C)	The maximum displacement(inch)		
	Analytical solution	Simulation result	Error value
0	0.0000	0.0000	
10	0.0168	0.0169	1.0%
20	0.0335	0.0339	1.0%
30	0.0503	0.0508	1.0%
40	0.0670	0.0677	1.0%
50	0.0838	0.0846	1.0%
60	0.1004	0.1015	1.0%
70	0.1171	0.1183	1.0%
80	0.1337	0.1351	1.0%
90	0.1503	0.1519	1.0%
100	0.1669	0.1686	1.0%
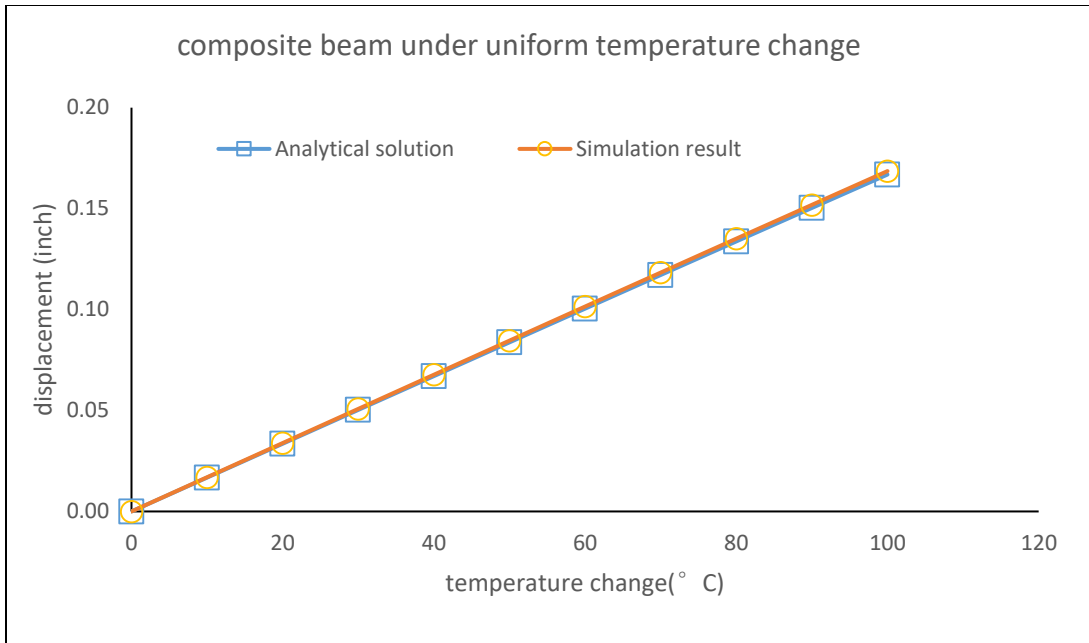
Figure II.2 Displacement in a composite beam under uniform temperature change

According to the Table II.2 and Figure II.2, the simulation matches the analytical solution quite well and the error values are below 2%. Thus, for the rest of parametric studies on bilayer plates under uniform temperature changes, numerical analyses will be considered.

2.2 Composite plates under thermal loadings

After the discussion about the composite beams under thermal loadings, we extend our work to 2D (two dimensional) planar models that can undergo various 3D (three dimensional) complex shapes. For 2D cases, we consider two- layered plates shown in Figure II.3, one as the substrate and another one as the patch. The size of the plate is 2.36 inch x 2.36 inch. We will vary the thickness of the plate and also the size of the patch, which will be discussed later. The two layer plates are tied together and they are

modeled as 2D shell models. The linear shell elements S4R are used for all the cases. After conducting the convergence study, we choose 0.02 inch as the element size for all the bilayer plate models. They can undergo deformation differently under uniform temperature change due to various factors like the thickness of the substrate, the stiffness of the substrate as well as the size of the patch in comparison to the substrate. In this section, parametric studies are conducted in order to examine several material and geometrical parameters that influence the deformed shapes of the bilayer plates.
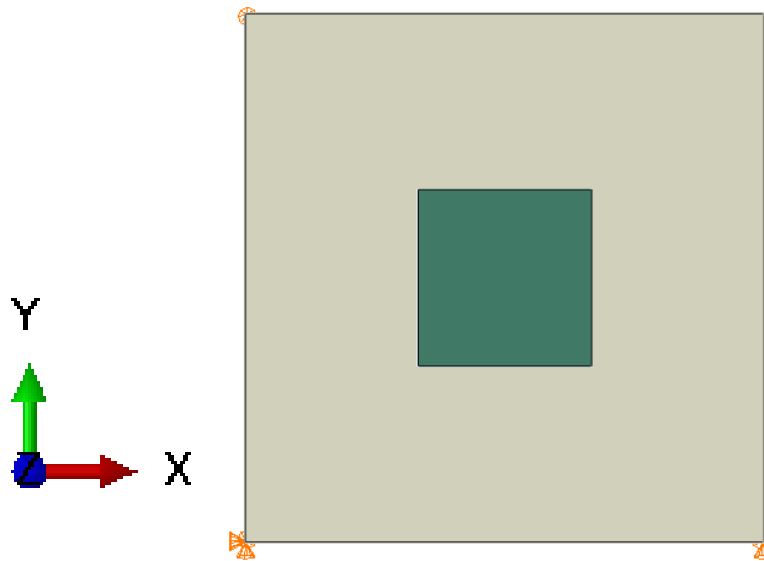
Figure II.3 The two-layered plates

2.2.1   Thickness

Thickness is an important factor that affects the bending stiffness of the structure. For a simple beam, the thicker the beam is, the harder it is to bend the beam in the thickness direction due to the increasing second moment of an area. When extended to a 2D planar cases, more variables are included in the problem, so models with different

13

thickness of the substrates are created to assess the effect of the thickness on the deformation of the structures under same thermal loadings.

The 2.36 inch x 2.36 inch square plates are introduced as the substrates and the thickness of the plates varies from 0.04 inch to 0.4 inch, while they are all tied to the center of a 0.79 inch x 0.79 inch square plate with 0.02 inch in thickness. The material property are shown in Table II.3. The uniform temperature change is 100°C and the boundary condition is to constrain three points as orange regions shown in Figure II.3 of the substrate to eliminate the rigid body motion of the model. The left bottom point is constrained in the displacement of all three directions, while the right bottom point and the left top point are constrained in the displacement of y and z direction and z direction, respectively. The displacement contours for substrates in different thickness are shown in Figure II.4.

The relationship between the maximum displacement and thickness are shown in Figure II.5. Based on the results, the relationship is not linear but following a third-order function of the thickness. Decreasing the thickness of the substrate can tremendously increase the flexibility of the composite plates, which is expected due to the decrease in the second moment of an area with regards to the bending axes. It is also seen that with thin substrates, smaller temperature changes are needed in order to induce deformations.

Table II.3 Properties for the material of the substrates and patches in different thickness

	Young's modulus	Poisson's ratio	Thermal expansion
Substrate	0.29×10^6 psi	0.2	150×10^{-6}
Patch	0.29×10^6 psi	0.2	5×10^{-6}

U, Magnitude
+2.357e-01
+2.161e-01
+1.964e-01
+1.768e-01
+1.571e-01
+1.375e-01
+1.178e-01
+9.821e-02
+7.857e-02
+5.892e-02
+3.928e-02
+1.964e-02
+0.000e+00

0.01 inch   0.02 inch

0.04 inch   0.08 inch
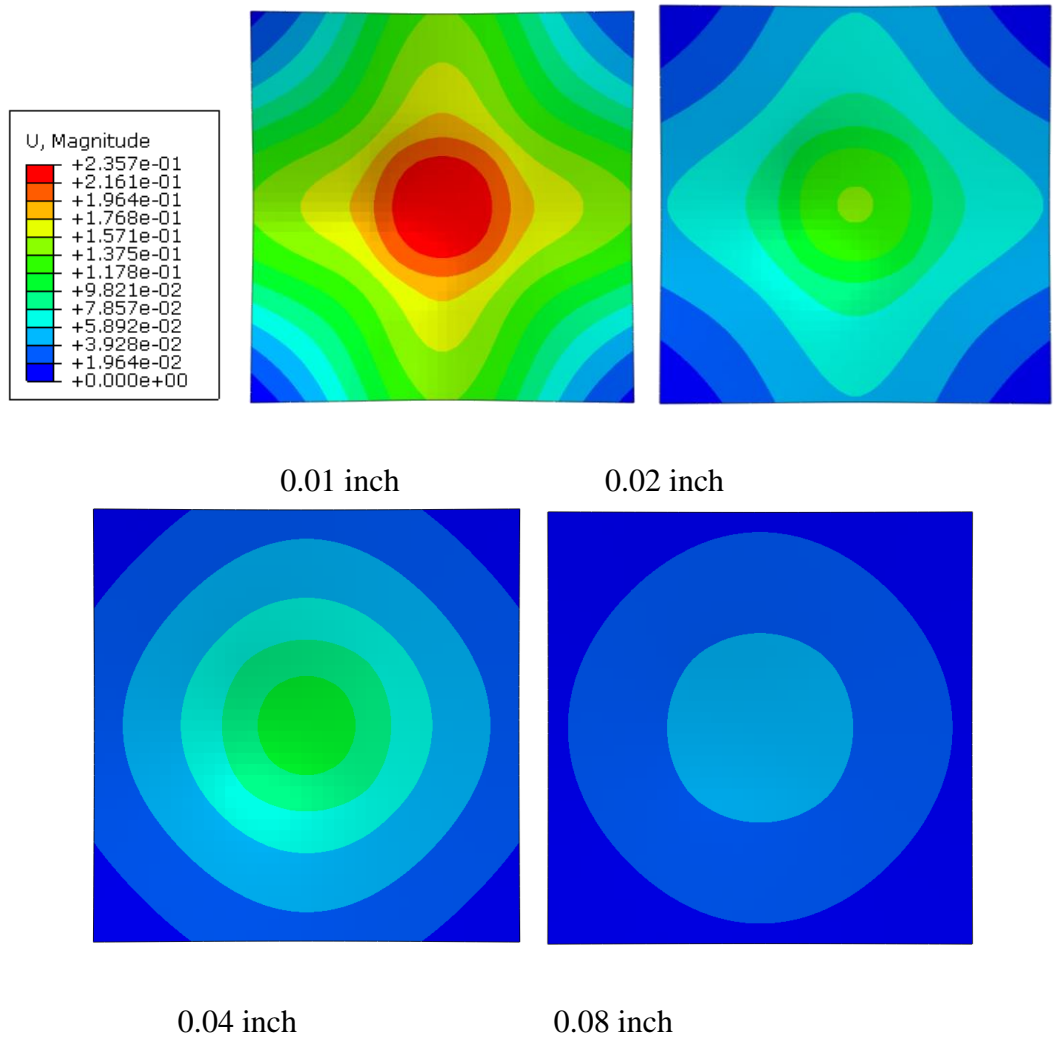
Figure II.4 Displacement contour for bilayer plates with different thickness in the sbustrates
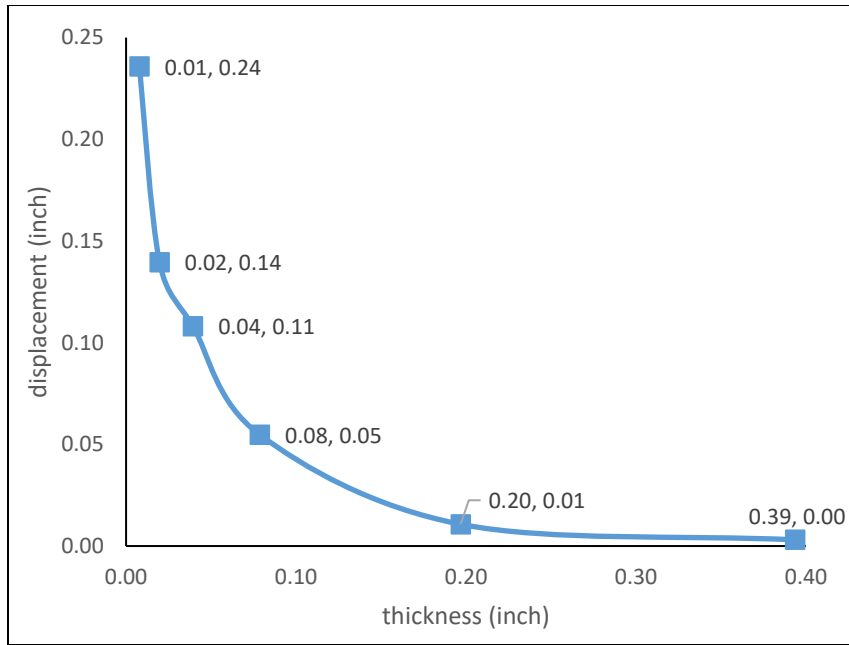
Figure II.5 The relation between the maximum displacement and the substrates thickness

2.2.2 Young's modulus

Young's modulus, also known as elastic modulus can measure the substrate's resistance to being deformed elastically under certain stress. It is also a significant parameter to determine the deformation of the structure. Thus, we use the same patch as before and a 2.36 inch x 2.36 inch square plate with 0.02 inch in thickness as the substrates, while the substrates have a wide range of Young's modulus (0.15e6 to 7.3e6 psi). The material property are shown in Table II.4. The uniform temperature change is 100°C and the boundary condition is the same as previous work to constrain three points in the bottom surface of the substrate to eliminate the rigid body motion of the model. The displacement contours for substrates in different Young's modulus are shown in Figure II.6.

The relationship between displacement and Young's modulus is denoted in Figure

16

II.7. The Figure II.7 is a semi-log plot and the Young's modulus is plotted on logarithmic scale. In this semi-log graph, the maximum displacement is approximately linear related to the Young's modulus. Higher elastic modulus leads to less compliant structures, as expected.

Table II.4 Properties for the material of the substrates and patches in different Young's modulus

	Young's modulus	Poisson's ratio	Thermal expansion
Substrate	varied	0.2	150×10^{-6}
Patch	0.29×10^6 psi	0.2	5×10^{-6}

1.45×10^5 psi 2.90×10^5 psi
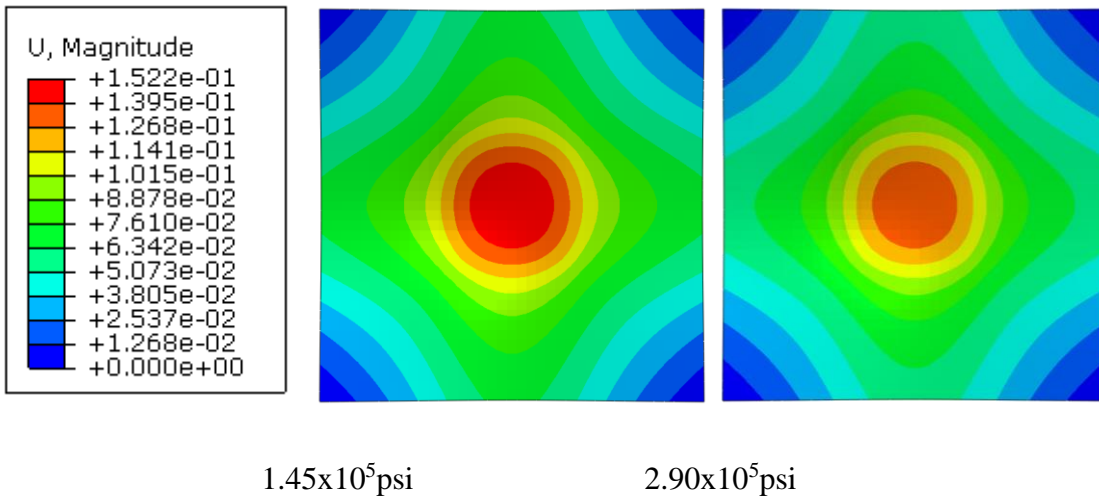
Figure II.6 Displacement contour for bilayer plates with the substrates in different Young's modules

7.25x10^5 psi   1.45 x10^{6}psi
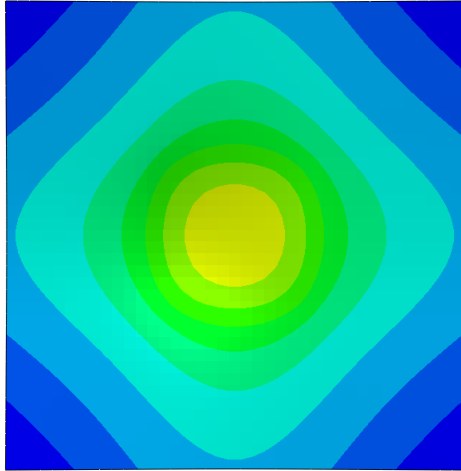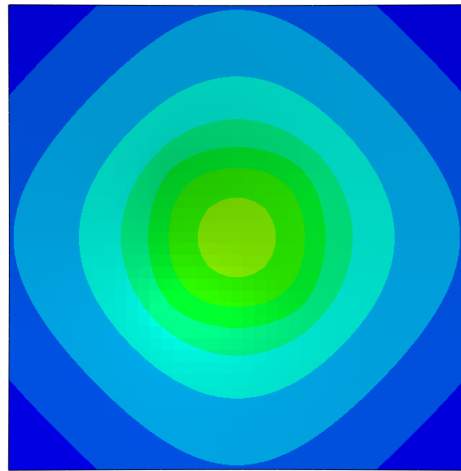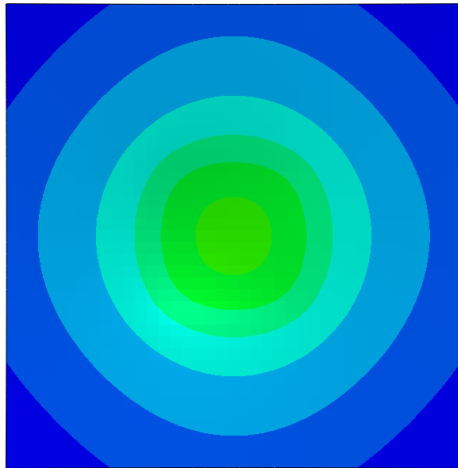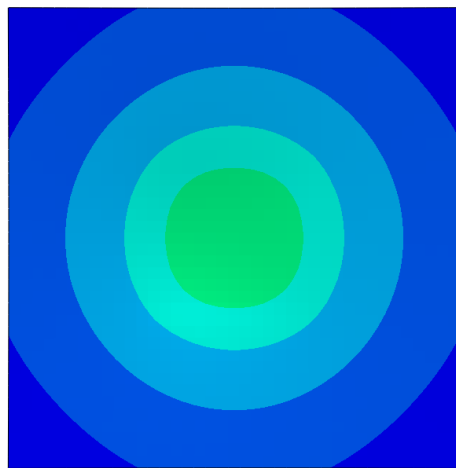
2.90 x10^{6}psi   7.25 x10^{6}psi

Figure II.6 Continued
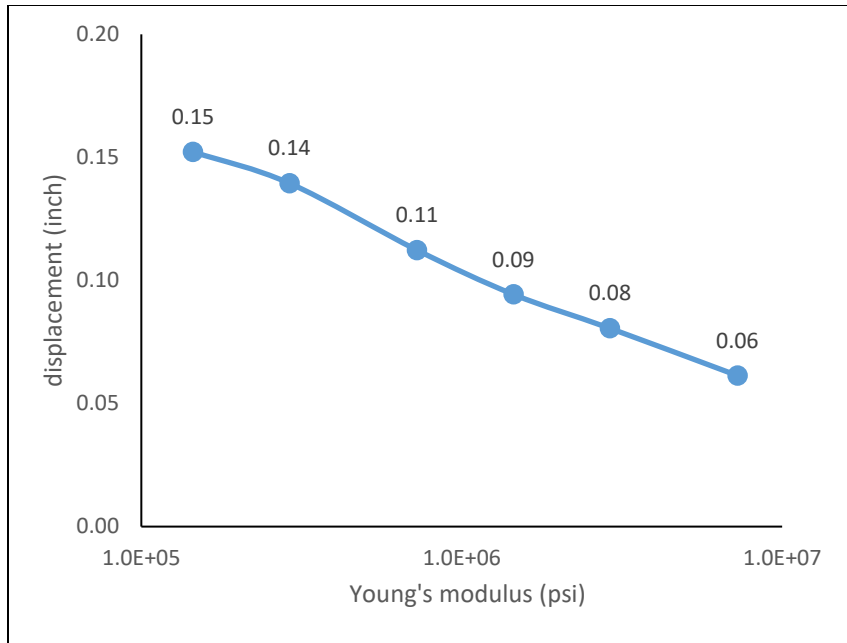
Figure II.7 The relation between displacement and the substrates young's modulus

2.2.3 Patch size

The size of the patch can also affect the deformations of the structures. The patch size is not an absolute value, but a relative one with regards to the size of the substrates. In order to examine the effect of ratios of the patch size to the substrate size on the overall deformations of the bilayer plates, we fix the substrate model following the previous examples, while we consider different sizes of the patch that is placed in the middle of the substrate. We use the length of the square patches as the factors. The material properties are shown in Table II.5. The uniform temperature change is 100°C and the boundary condition is to constrain three points in the bottom surface of the substrate to eliminate the rigid body motion of the model, as discussed previously. The displacement contours for different patch seizes are shown in Figure II.8. According to the Figure II.9, the maximum displacements of the plates are positive correlation with

19

the patch size. The larger area with high displacement gradients due to a thermal stimulus leads to higher bending deformations.

Table II.5 Properties for the material of the substrates and patches in different patch sizes

	Young's modulus	Poisson's ratio	Thermal expansion
Substrate	$0.29\text{x}10^6$ psi	0.2	$150\text{x}10^{-6}$
Patch	$0.29\text{x}10^6$ psi	0.2	$5\text{x}10^{-6}$

| 1.18 inch	0.94 inch

0.71 inch	0.47 inch	0.24 inch
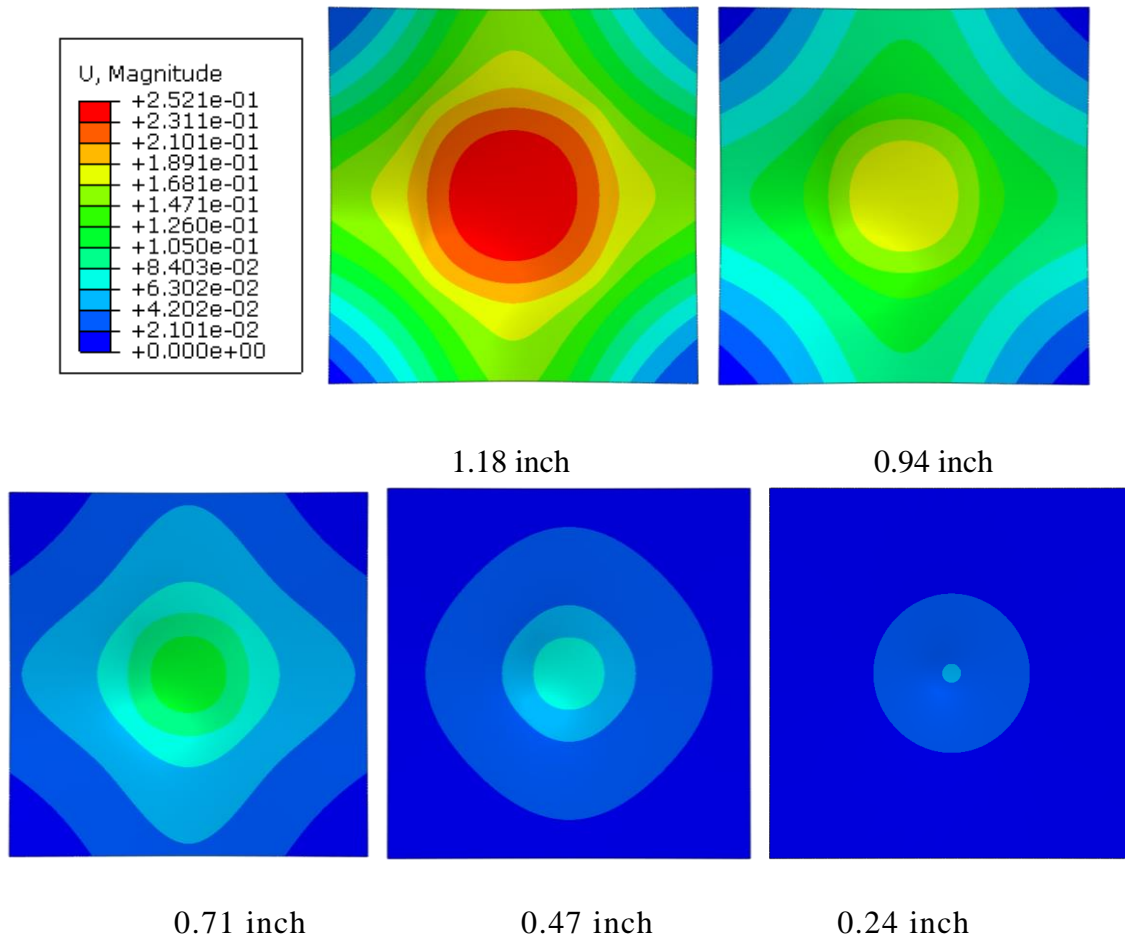
Figure II.8 Displacement contour for bilayer plates with the different patch size
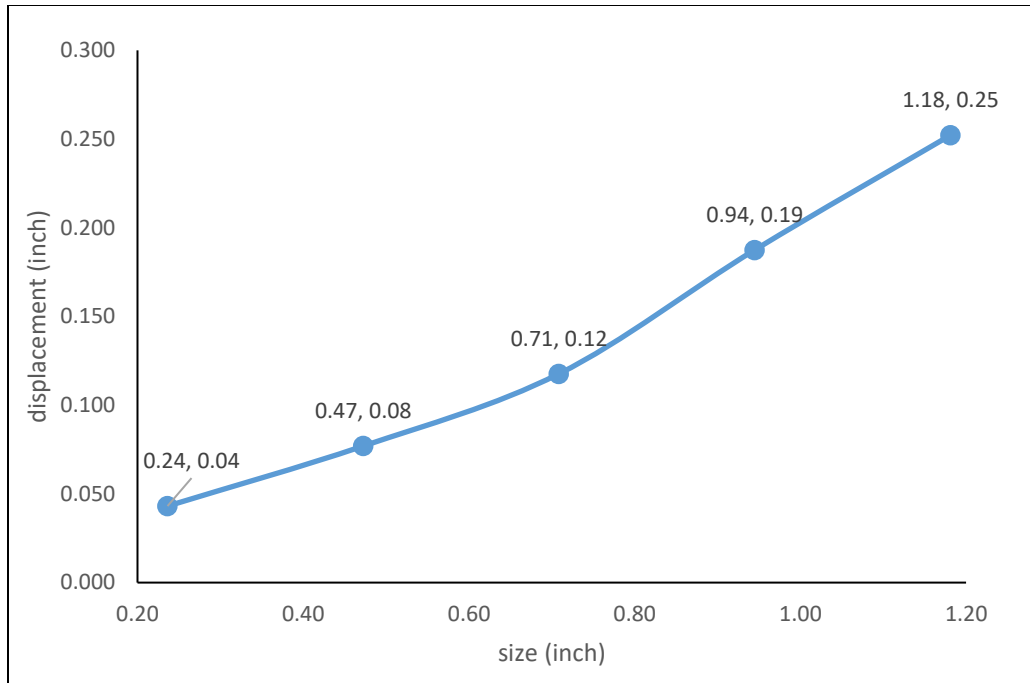
Figure II.9 The relation between displacement and the patch size

2.2.4   Patch shapes and patch locations

In the previous works, we have all plates in square and all patches placed in the center of the substrates, so all deformations have four symmetric planes. If we want to get the unsymmetrical geometrical configurations, changing patch shapes and patch locations are two ways to achieve the goal.

Patch shape

There are various shapes which can be applied in the patches. For the square substrates, instead of having four sides deformed equally, we can change the square patches into the rectangle ones to make each opposite two sides deformed equally. In this way, comparing the displacement of the sides can be used to figure out the effects

of the patch shape on the deformation.

A same substrate plate (2.36 inch x 2.36 inch x 0.02 inch) is used and all patches are of same volume (3.1×10^{-3} in^3). We have five kinds of patches and the parameters are shown in Table II.6.

Table II.6 The dimensions of the patches

	Length/inch	Width/inch	Thickness/inch
1	1.97	0.0789	0.020
2	0.984	0.157	0.020
3	0.787	0.197	0.020
4	0.492	0.315	0.020
5	0.394	0.394	0.020

All the patches are still tied to the center of the substrates and the material properties are shown in Table II.7. The uniform temperature change is 100°C and the boundary condition is to constrain three points in the bottom surface of the substrate to eliminate the rigid body motion of the model, as discussed previously. The displacement contours for different patch shapes are shown in Figure II.10. Based on Figure II.10, we can see the plates with patch with the smallest length and width aspect ratio have smallest deformation. Instead, the patch with higher length and width aspect ratio can not only account for largest bending in the length direction, but also eliminate the bending in the width direction because there are large area with high displacement gradient along the length direction. It is beneficial for the plates bending in one direction.

Table II.7 Properties for the material of the substrates and patches in different patch shape

	Young's modulus	Poisson's ratio	Thermal expansion
Substrate	0.29×10^6 psi	0.2	150×10^{-6}
Patch	0.29×10^6 psi	0.2	5×10^{-6}

Shape_1   Shape_2

Shape_3   Shape_4   Shape_5
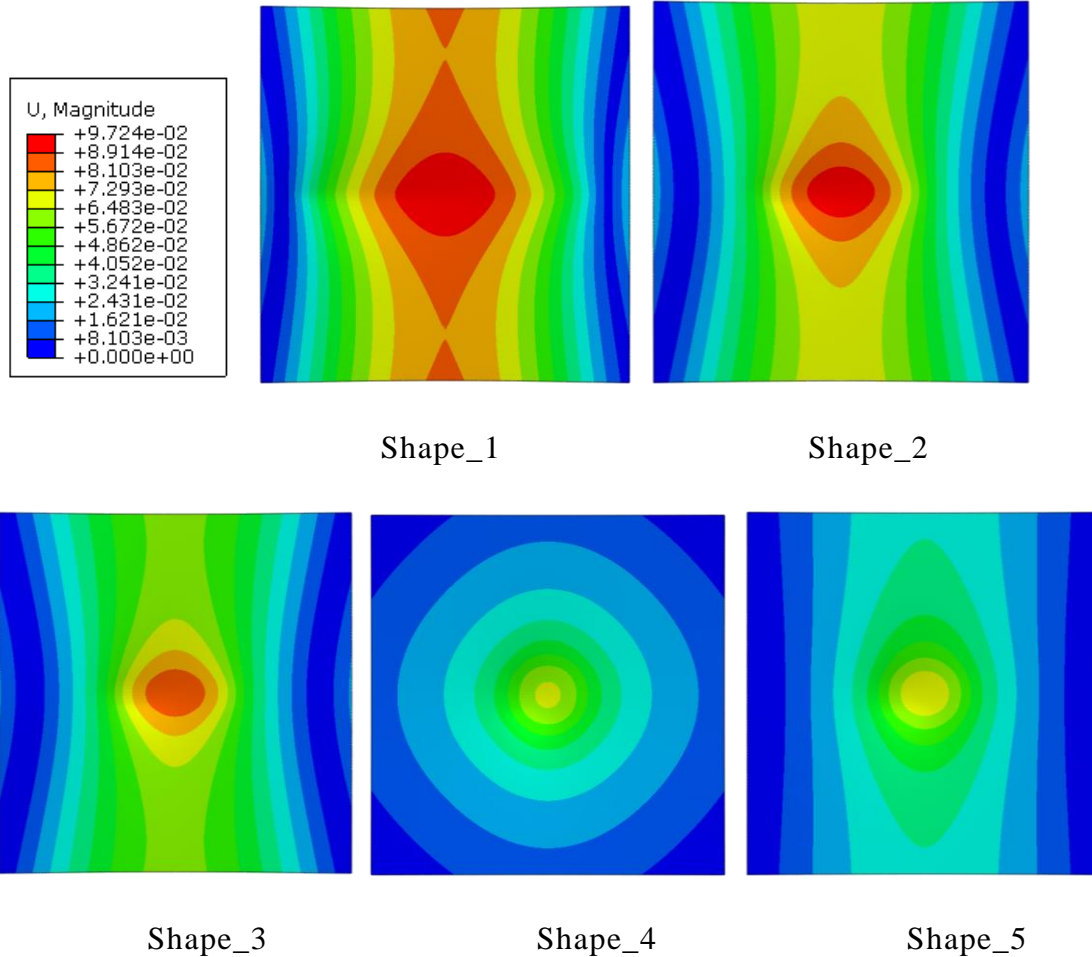
Figure II.10 Displacement contour for bilayer plates with patches in different shapes

Patch locations

Instead of placing all the patches in the center of the substrates, patches in other

locations can cause distinct unsymmetrical deformations. A 2.63 inch x 2.63 inch x 0.02

inch substrate can be divided to 3x3 grid like in Figure II.11.
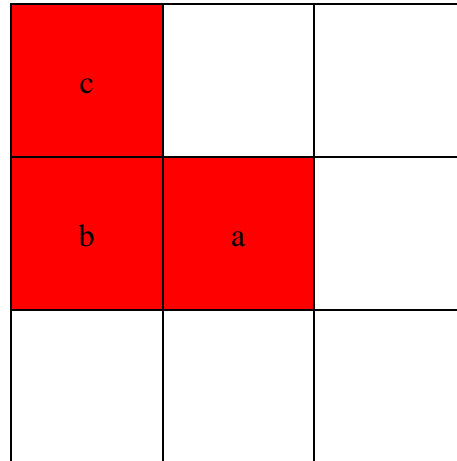
Figure II.11 The divided substrate model

Each grid is a 0.79 inch x 0.79 inch square, so the patch size we use is 0.79 inch x 0.79 inch x 0.02 inch. For the nine grids, there are only three independent grids shown in the red because the square is symmetrical. Thus, we take these three grids as the patch locations. As is shown in Figure II.12, the center-located patch can deformed the largest. Also, the locations further from the patches will deform much less than the patch areas do. Because the patch is still square shape, the displacement contours are all symmetrical but with the respect of different axis.
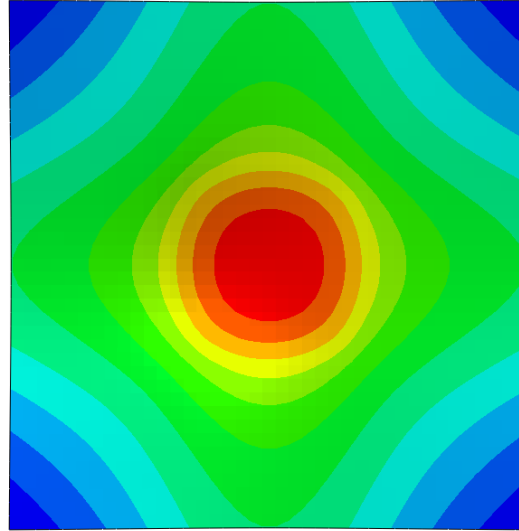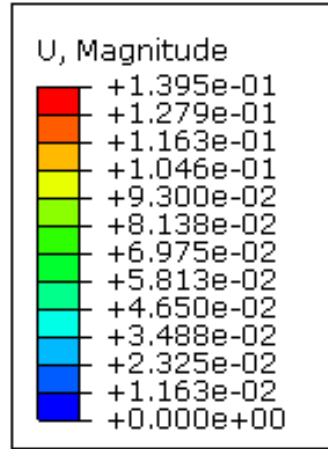
Location a
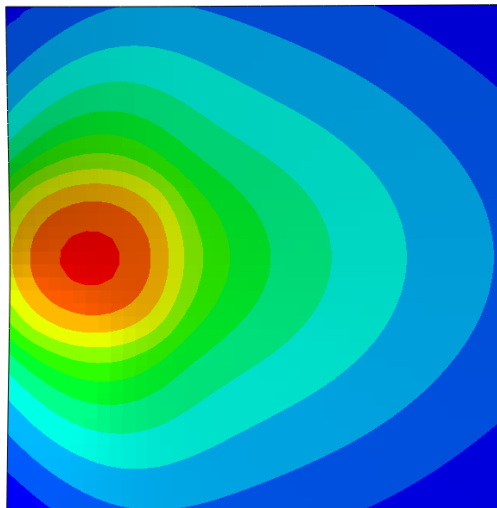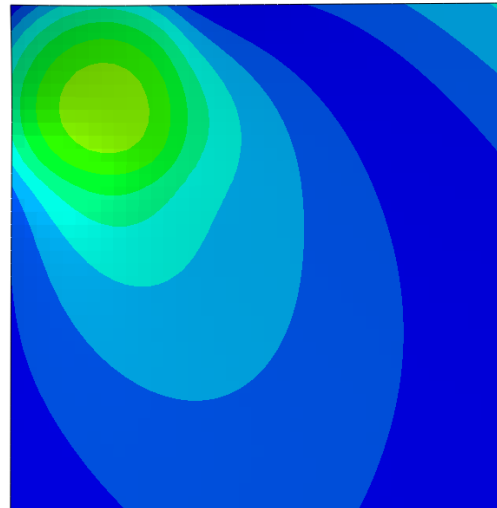
Location b   Location c

Figure II.12 Displacement contour for bilayer plates with different patch locations

2.3 Application

Based on above parametric studies, we have gained some basic understanding on

how the deformation of the bilayers changes with various material and geometrical

parameters. The key component in achieving large out of plane deformation by having large displacement gradients through the thickness of the bilayers. The results from the present analyses can be applied to smart structures that can respond to the variations of the environment.

A smart plate as an example is illustrated in the following work. A star shape plate is created in Figure II.13. The final purpose is that the star plate can fold itself like a flower under uniform temperature change. According to the previous works, slender beams in 2.36 inch x 0.394 inch x 0.020 inch are designed and they are placed close to the vertexes of the star shown in Figure II.13.

Figure II.13 The star-shaped smart plate model

The model is created in shell element S4R and the element size is 0.02 inch. The material property are shown in Table II.8. The uniform temperature change is 50°C and the boundary condition is to constrain three points as the orange region shown in Figure II.13 in the bottom surface of the substrate to eliminate the rigid body motion of the model, as discussed previously. According to Figure II.14, the star shape plate with

26

these patches fold dramatically under uniform temperature changes and basically achieve the original desired shape.

Table II.8 Properties for the material of the substrates and patches in the star application

	Young's modulus	Poisson's ratio	Thermal expansion
Substrate	0.29×10^6 psi	0.2	150×10^{-5}
Patch	0.29×10^6 psi	0.2	5×10^{-6}
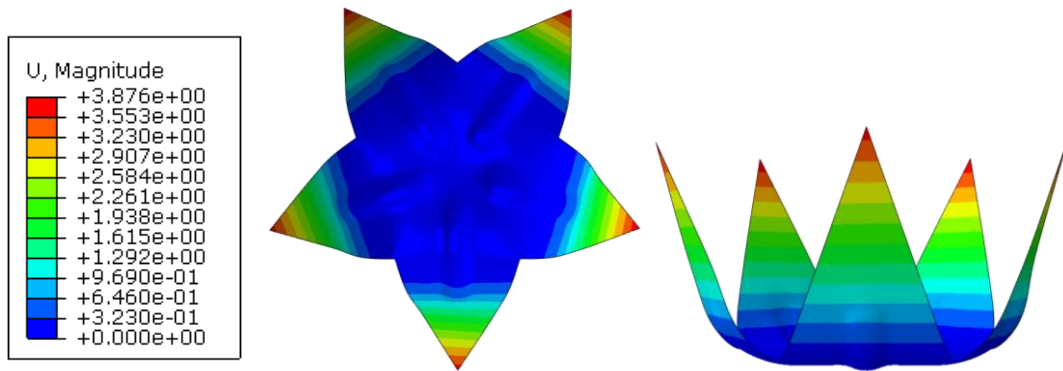
Figure II.14 The displacement contour for the deformed star shape plates

We take a saddle shape in Figure II.15 as another example to see how the smart plate can deform into the desired configurations. As the hyperbolic paraboloid, the saddle shape is doubly ruled surface with the opposing two sides bending in the one direction and other two sides in another direction. Let us consider a same thin plates as before with the size of 2.37 inch x 2.37 inch x 0.02 inch. The opposing side of the plates should bend symmetrically in terms of the origin point, so we can have a slender beam tied on the top surface along the diagonal to achieve the symmetrical bending in this direction like Figure II.16.

27
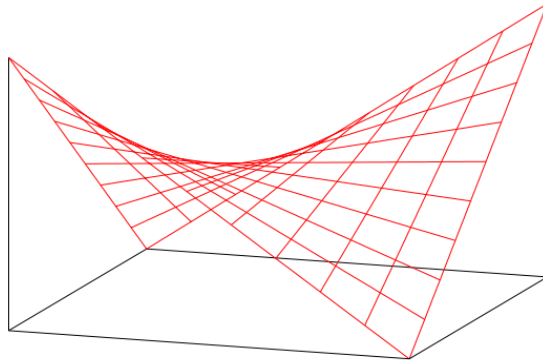
Figure II.15 The saddle shape example
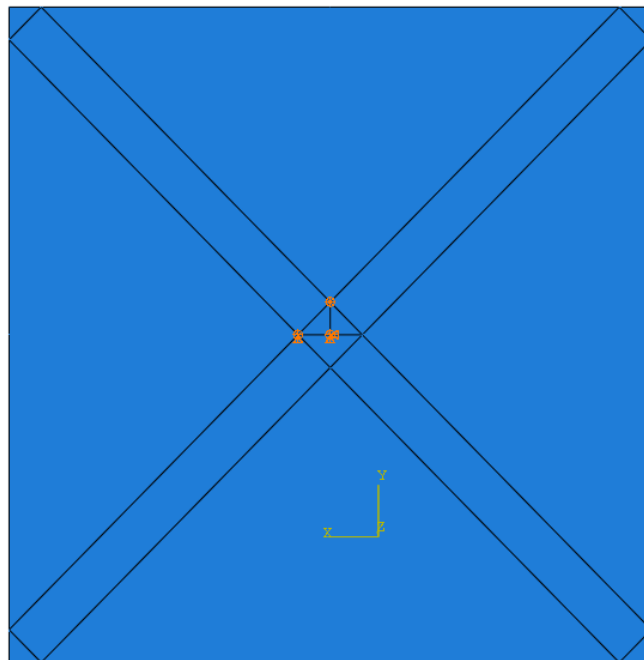
Figure II.16 The designed bilayer plate model

A shell FE model is created with element S4R and the element size is 0.02 inch. The property for the materials are shown in Table II.9.The uniform temperature change is

50°C and the boundary condition is to constrain three points in the center of the substrate shown as orange region in Figure II.16 to eliminate the rigid body motion of the model, as described before.

Table II.9 Properties for the material of the substrates and patches in saddle shape

	Young's modulus	Poisson's ratio	Thermal expansion
Substrate	0.29×10^6 psi	0.2	150×10^{-5}
Patch	0.29×10^6 psi	0.2	5×10^{-6}
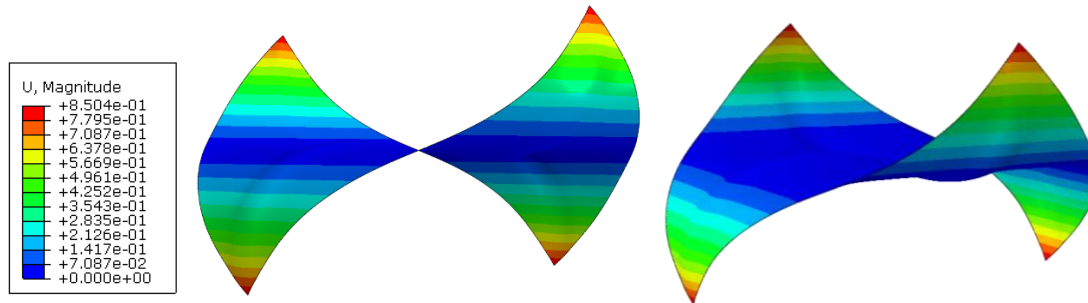
Figure II.17 Displacement contour for the saddle shape

According to Figure II.17, the plate with the patches can achieve almost the sadlle shape under thermal loadings. Bilayer plates under thermal loadings have great potiential to achieve complicated shapes.

Instead of designing each patch for every application example, we could have same patch arranged in a certain sequence to achieve the desired configurations. A 15 inch x15 inch substrate is still used as before and has been divided into 15x15 grids shown in the Figure II.18. For the Model_1 shown in Figure II.19, we use the square patches placed in a certain sequence. The red region is the patch placed on the top surface and

the green region is the patch placed on the bottom surface. In Model_2, square patches have been changed into the patch style used in the saddle shape example, which have one slender beam placed on the diagonal on the top surface and another on the bottom surface. Rather than having discrete patch locations shown in the Model_1 and Model_2, we can place continous patches in the substrate shown in Model_3. The element type for each model is S4R and the element size is 0.02 inch. The property for the materials are shown in Table II.10. The uniform temperature change is 100°C. The boundary conditions for Model_1 and Model_3 are both to constrain the three points illustrated before to eliminate the rigid body motion. For Model_2, we constrain the center part of the substrate in all directional displacements.
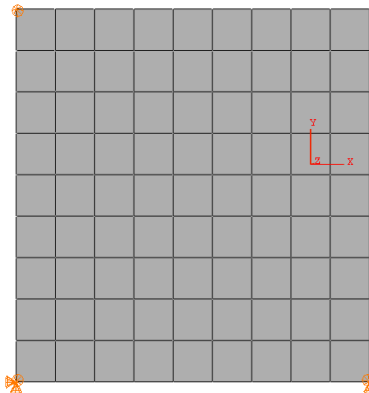
Figure II.18 The divided substrate
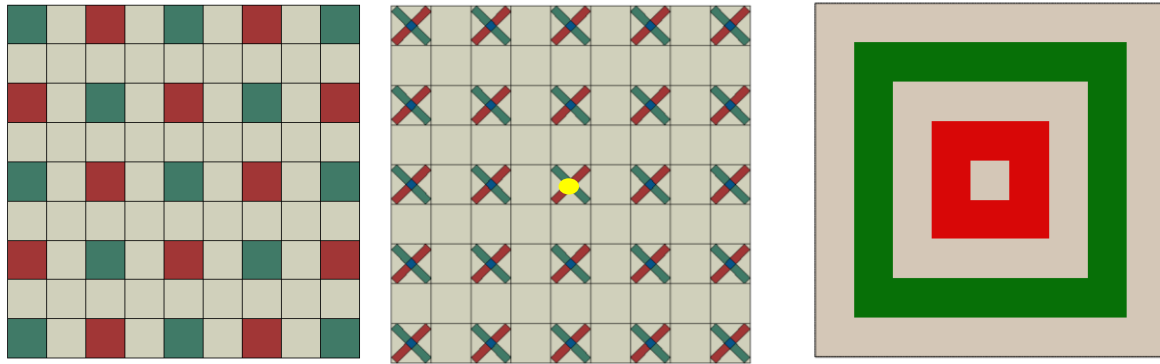
Model_1   Model_2   Model_3

Figure II.19 Application models

Table II.10 Properties for the material of the substrates and patches in continous patches

	Young's modulus	Poisson's ratio	Thermal expansion
Substrate	0.29×10^6 psi	0.2	150×10^{-5}
Patch	0.29×10^6 psi	0.2	5×10^{-6}
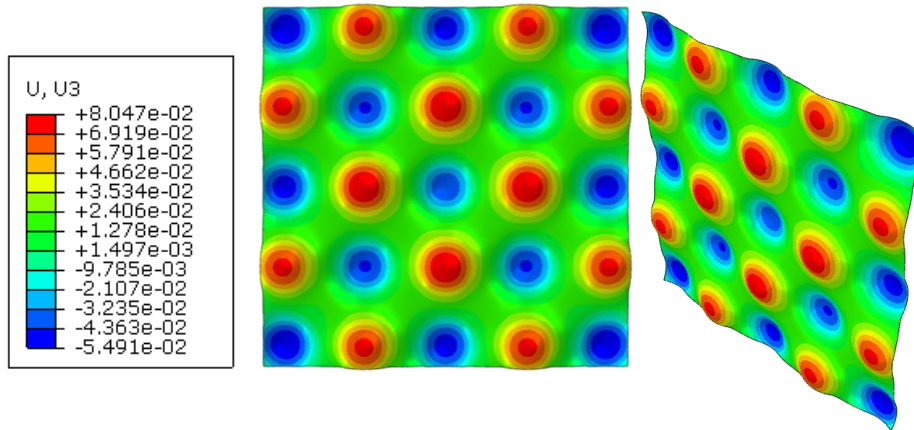
Figure II.20 Model_1 displacement contour (inch)
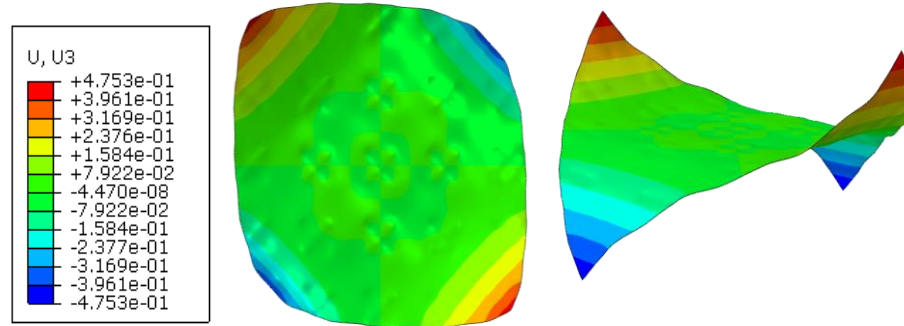
Figure II.21 Model_2 displacement contour (inch)
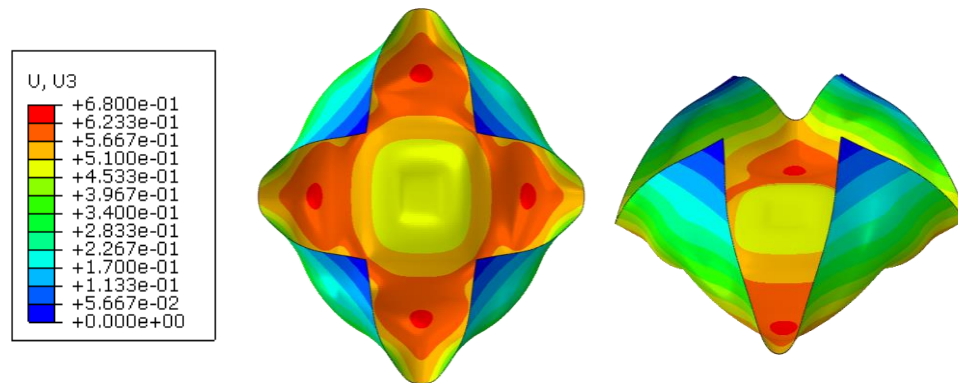
Figure II.22 Model_3 displacement contour (inch)

According to the Figure II.20, the Model_1 deformed like waves with concaves and convexities on the patch locations as predicted. In Figure II.21, the overall deformed shape for the Model_2 is still a saddles shape but with some slight deformation occurred on the patch locations. From Figure II.22, the plate folds itself dramatically due to the out layer patches, while there is a convex shown in the center of the plate for the inner layer patches.

According to all examples shown above, the bilayer composite plates have great potentials in achieving the desired complicate configurations.

CHAPTER III

ARCHITECTURE KERFING PATTERNS UNDER MECHANICAL LOADINGS

Relief cutting is a new technique in order to transform a relatively stiff plate to a more flexible and compliant plate, which can be accomplished by a wide variety of cutting patterns. It is quite interesting to see that the rigid planar surface can have such great flexibility with theses cuttings, so further study is conducted in order to understand the mechanisms underlying mechanical deformations on these kerf structures. In this study, we choose one of the most common square patterns (Interlocked Archimedean Spirals) as the kerfing pattern. The advantage of this pattern is that it is relative easy to arrange them to achieve desired deformations.

ABAUQS finite element (FE) analyses are used in order to study the deformation of the kerfing patterns. We start with a unit-cell model and study several deformations, i.e., axial, equibiaxial, bending, and twisting, of the unit cell. First we compared the responses from using three-dimensional (3D) continuum element and beam element in generating the unit-cell model. The 3D continuum element allows for generating the unit-cell with precise shapes and sizes, including detailed model of the patterns. However, it can be computationally expensive when one want to generate large scale panel with complex deformed shapes. The use of beam element will definitely reduce computational cost, especially when large scale structural analyses are considered, with a caveat that detailed geometrical shapes and sizes cannot be incorporated in the analyses. Later we conduct parametric studies on understanding the effect of cut

densities on the overall deformation of the unit-cell using the beam element. An experimental test is performed on unit-cell models with different cut densities subjected to a uniaxial deformation. Responses from the experiments and FE analyses are compared. Finally, large scale plate structures with different arrangements of unit-cells of various cut densities are analyzed and the deformed shapes of these structures due to mechanical stimulus are studied.

3.1 Responses of Unit-cell with 3D continuum and beam elements

Three-dimensional (3D) continuum elements are often computationally expensive, especially in large panels consisting of repeated unit sections like what we will design later. Alternatively, we can consider structural elements, such as beam or frame element, instead of the continuum ones. However, for the result to be accurate, we need to demonstrate that the structural element can also capture the deformations of the structure well.

Initially, element type frame3d is chosen to capture the continuum model, but, in ABAQUS, frame element can only output forces, moments, elastic strains and curvatures instead of stress and displacement which is important indicators for the analysis in our cases. Thus, instead of a frame element, beam element is used for the following works. Several numerical tests are conducted on the same unit section using beam element and continuum element to compare their behaviors.

To create a beam model, simplifications of the original models are needed. The 3D model is designed in SolidWorks based on the actual design parameters provided by the architecture lab. The centerline of each cut pattern in the 3D model is represented as a

34

prismatic beam. This way the 3D continuum model is transferred into a planar model which is then imported into ABAQUS for the stress analysis. In the following works, all continuum models are created in 8-node linear brick element C3D8 and all beam models are in linear beam element B31. From the convergence study (see Appendix A), the element size for the beam model is 0.0004 inch and the total element number is 20576, while, for the continuum model, the element size is 0.001 inch and the element number is 58240. Both models with 3D continuum and beam elements are now used to study the responses under uniaxial extension, biaxial extension, bending and twisting. The MDF is modeled as linear elastic and isotropic material with elastic modulus of 0.58×10^6 psi, Poisson's ratio of 0.25 and tensile strength of 2.6×10^3 psi.

3.1.1   Case 1 uniaxial extension

In the uniaxial extension, the boundary condition is to constrain the top endpoint in all direction of the displacements and a displacement loading is applied at the bottom endpoint along the vertical direction in the beam model. In the continuum model, the boundary condition and loading are the same, but they are applied on the end faces instead of points. Loading is applied until the maximum stress reaches the ultimate tensile stress of the MDF. The stress contour and displacement contour for these three unit sections under maximum loading are shown in Figure III.1 and Figure III.2, respectively. The analysis time for continuum model in uniaxial extension simulation is 39s, more than twice of that for the beam model (15s).

According to Table III.1 and Figure III.3, under uniaxial extension, the continuum model and the beam model give relatively close behaviors with less than 10% difference.

Figure III.1 Displacement contour for beam and continuum models in case 1

Figure III.2 Stress contour for beam and continuum models in case 1

Table III.1 Results for beam and continuum models in case 1

case1_uniaxial extension				
continuum model		beam model		error value
force/lbf	displacement/inch	force/lbf	displacement/inch	
2.25E-05	1.85E-07			
2.25E-04	1.85E-06	1.12E-03	1.01E-05	
2.25E-03	1.85E-05	2.25E-03	2.02E-05	9%
1.12E-02	9.29E-05	1.12E-02	1.01E-04	9%
1.69E-02	1.39E-04	1.69E-02	1.52E-04	9%
2.25E-02	1.85E-04	2.25E-02	2.02E-04	9%
5.62E-02	4.65E-04	5.62E-02	5.08E-04	9%
1.12E-01	9.29E-04	1.12E-01	1.01E-03	9%
1.69E-01	1.39E-03	1.69E-01	1.52E-03	9%
2.25E-01	1.86E-03	2.25E-01	2.03E-03	9%
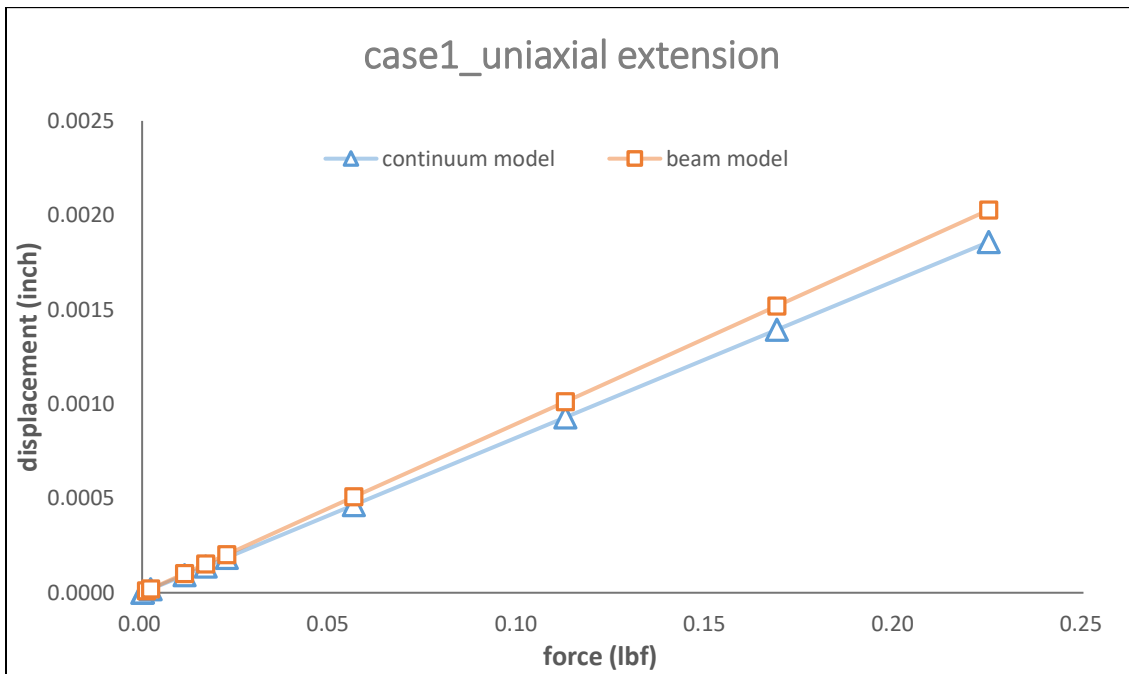
Figure III.3 The relation between displacement and force for beam and continuum models in case 1

37

3.1.2 Case 2 biaxial extension

In the equibiaxial extension, the boundary condition is to constrain the bottom and right endpoints in all direction of the displacement and a displacement loading is applied at the left and top endpoints along the vertical direction in the beam model. In the continuum model, the boundary condition and loading are the same, but they are applied on the end faces instead of points. The stress contour and displacement contour for these three unit sections under maximum loading are shown in Figure III.4 and Figure III.5, respectively. The analysis time for the continuum model under biaxial extension simulation is 29s, about twice of that for the beam model (15s).

According to Table III.2 and Figure III.6, the performance in biaxial extension for the continuum model and the beam model are nearly the same. Including the uniaxial extension case discussed before, the beam model can capture the stretching behaviors of the continuum model well.
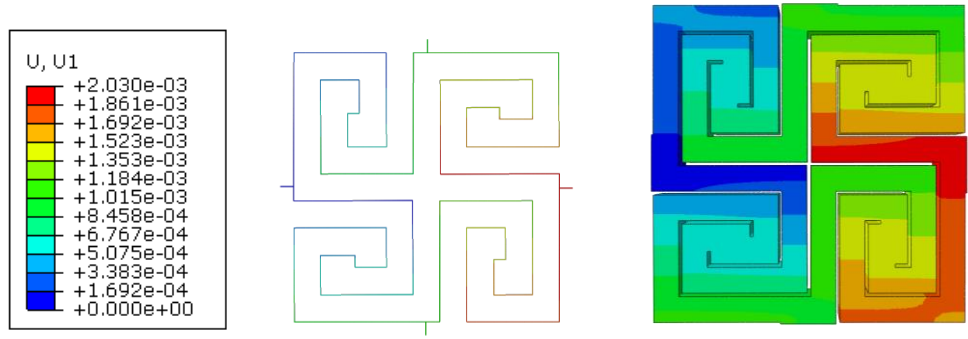

Figure III.4 Displacement contour for beam and continuum models in case 2
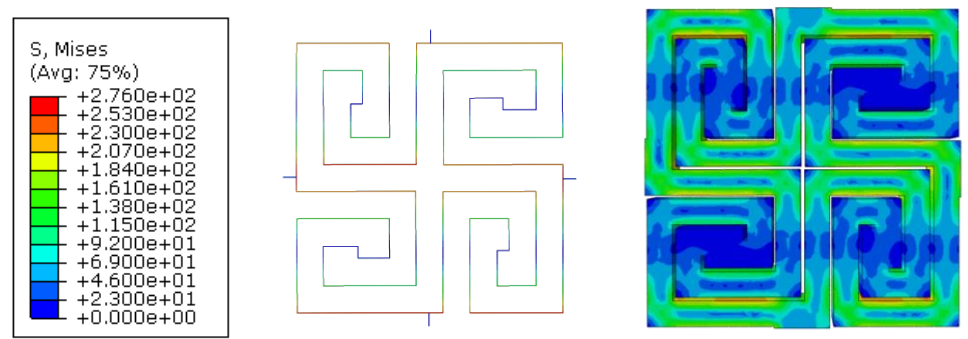
Figure III.5 Stress contour for beam and continuum models in case 2

Table III.2 Results for beam and continuum models in case 2

case2_biaxial extension				
continuum model		beam model		
force/lbf	displacement/inch			error value
2.25E-05	4.84E-07	force/lbf	displacement/inch	
2.25E-04	4.84E-06	1.12E-03	2.51E-05	
2.25E-03	4.84E-05	2.25E-03	5.00E-05	3.33%
1.12E-02	2.43E-04	1.12E-02	2.50E-04	3.17%
1.69E-02	3.64E-04	1.69E-02	3.76E-04	3.31%
2.25E-02	4.84E-04	2.25E-02	5.00E-04	3.33%
5.62E-02	1.21E-03	5.62E-02	1.25E-03	3.31%
1.12E-01	2.43E-03	1.12E-01	2.50E-03	3.31%
1.69E-01	3.63E-03	1.69E-01	3.68E-03	1.37%
2.25E-01	4.84E-03	2.25E-01	5.00E-03	3.33%

Figure III.6 The relation between displacement and force for beam and continuum models in case 2

3.1.3   Case 3 twisting

In twisting, the boundary condition is to constrain the left and right endpoints in all direction displacement and forces are applied at the top and bottom endpoints in different out-plane directions in the beam model. In the continuum model, the boundary condition and loading are the same, but they are applied on the end faces instead of points. The stress contour and displacement contour for these three unit sections under maximum loading are shown in Figure III.7 and Figure III.8, respectively. The analysis time for the continuum model in twisting simulation is 34s, more than twice of that for the beam model (14s).

According to Table III.3 and Figure III.9, the differences in the analyses with beam and continuum 3D elements are less than 9%, which is reasonably well.
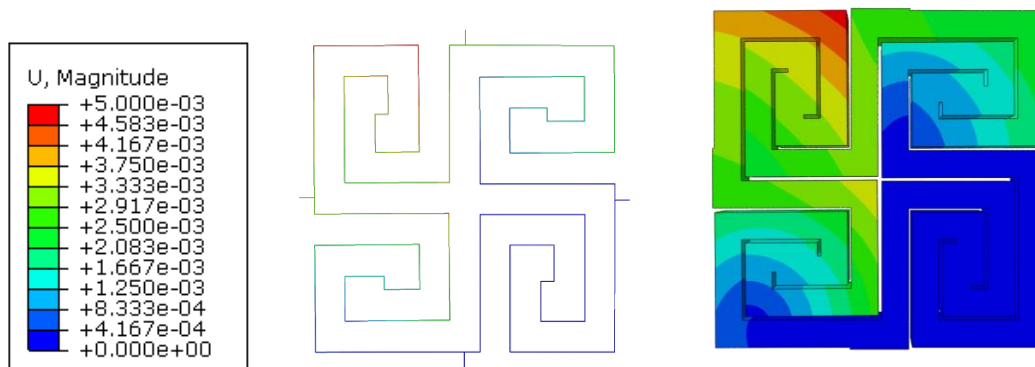
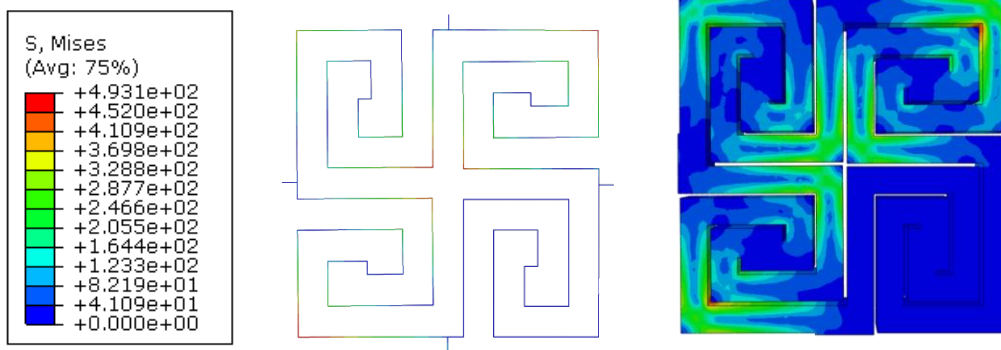**Figure III.7 Displacement contour for beam and continuum models in case 3**

Figure III.8 Stress contour for beam and continuum models in case 3

Table III.3 Results for beam and continuum models in case 3

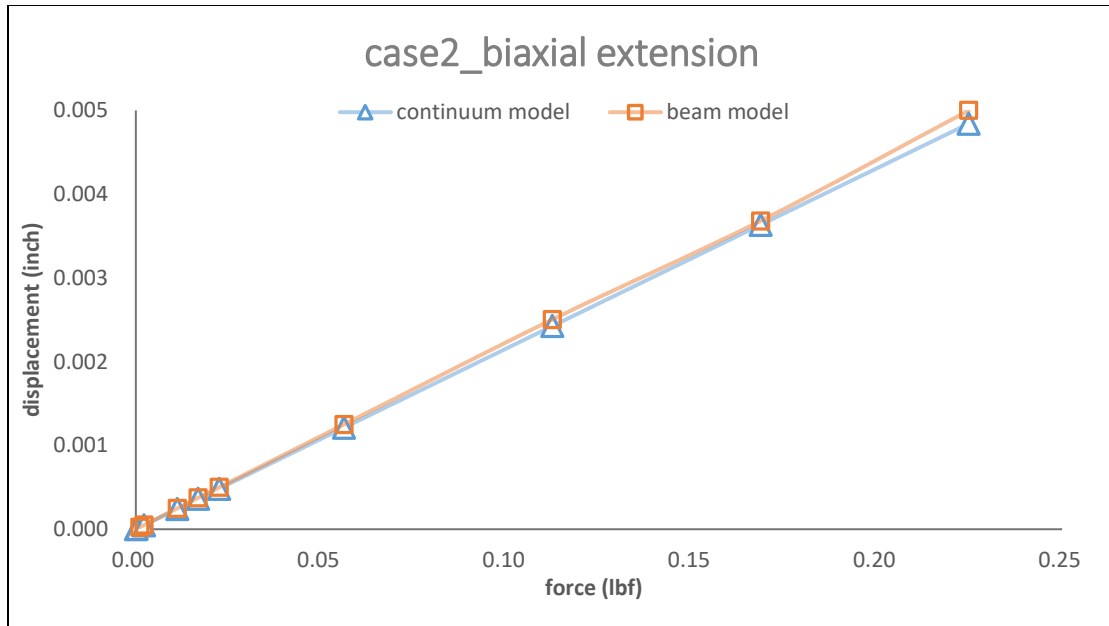| case3_twisting				
continuum model		beam model		error value
force/lbf	displacement/inch	force/lbf	displacement/inch	
2.25E-06	5.16E-07			
2.25E-05	5.16E-06	1.12E-04	2.38E-05	
2.25E-04	5.16E-05	2.25E-04	4.76E-05	7.63%
2.25E-03	5.16E-04	2.25E-03	4.76E-04	7.63%
1.12E-02	2.58E-03	1.12E-02	2.38E-03	7.93%
2.25E-02	5.16E-03	2.25E-02	4.76E-03	7.63%
5.62E-02	1.30E-02	5.62E-02	1.19E-02	8.21%
1.12E-01	2.59E-02	1.12E-01	2.37E-02	8.50%
1.69E-01	3.89E-02	1.69E-01	3.55E-02	8.80%
2.25E-01	5.20E-02	2.25E-01	4.72E-02	9.09%
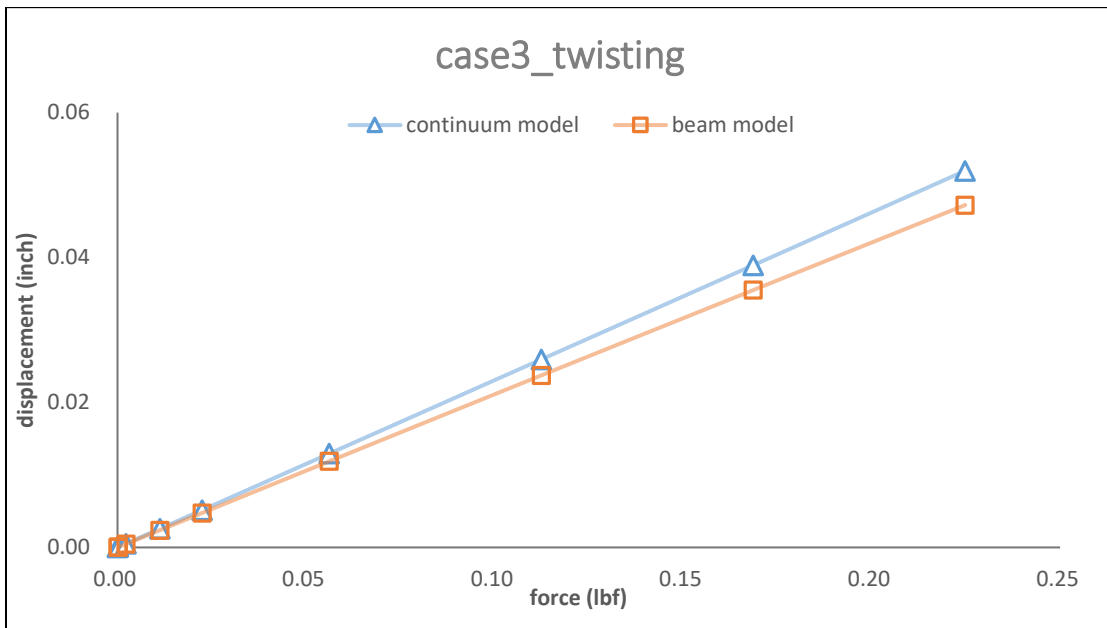
**Figure III.9 The relation between displacement and force
for beam and continuum models in case 3**

3.1.4 Case 4 bending

In twisting, the boundary condition is to constrain the left and right endpoints in all directions of the displacement and forces are applied at the top and bottom endpoints in same out-plane directions in the beam model. In the continuum model, the boundary condition and loading are the same, but they are applied on the end faces instead of points. The stress contour and displacement contour for these three unit sections under maximum loading are shown in Figure III.10 and Figure III.11, respectively. The analysis time for continuum model in uniaxial extension simulation is 35s，more than twice of that for the beam model (15s). According to the analysis time from the four cases, the beam model can reduce half or even more time during the simulation procedure in contrast to the continuum model.

According to Table III.4 and Figure III.12, for bending behaviors, the difference between the continuum model and beam model is a little larger than the stretching behaviors. Beam element can capture the in-plane deformations better than the out-plane ones.
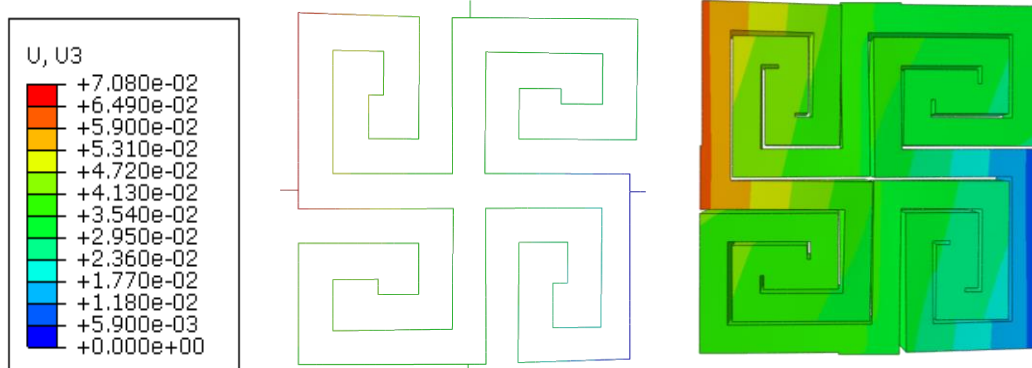
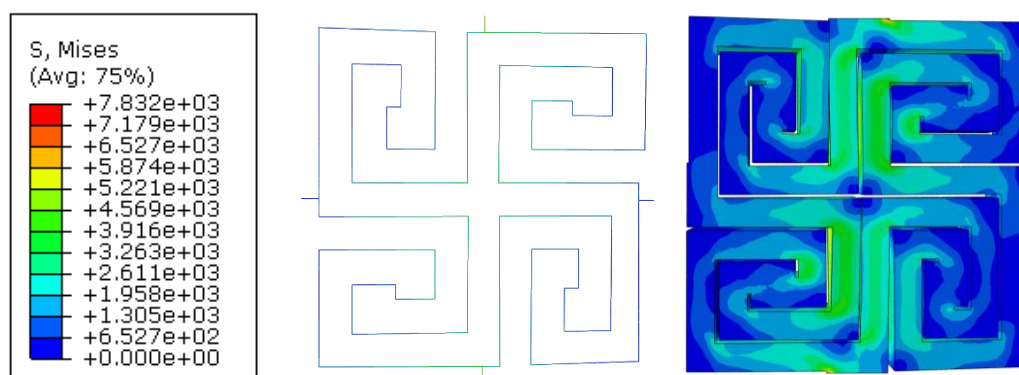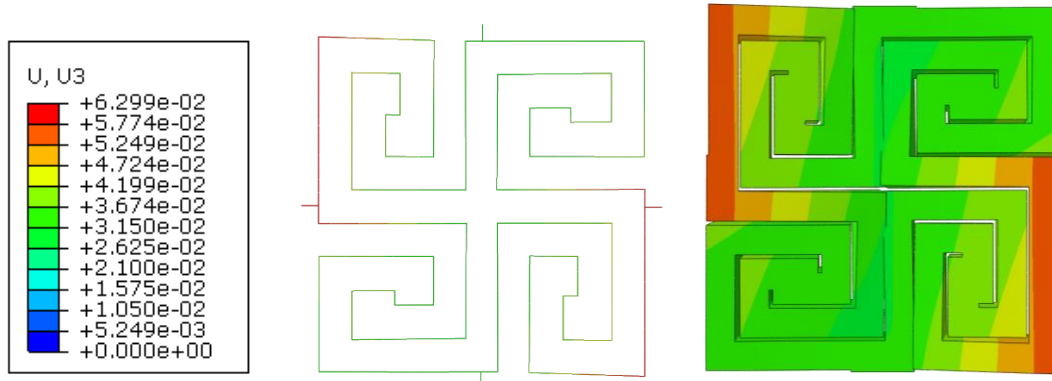**Figure III.10 Displacement contour for beam and continuum models in case 4**
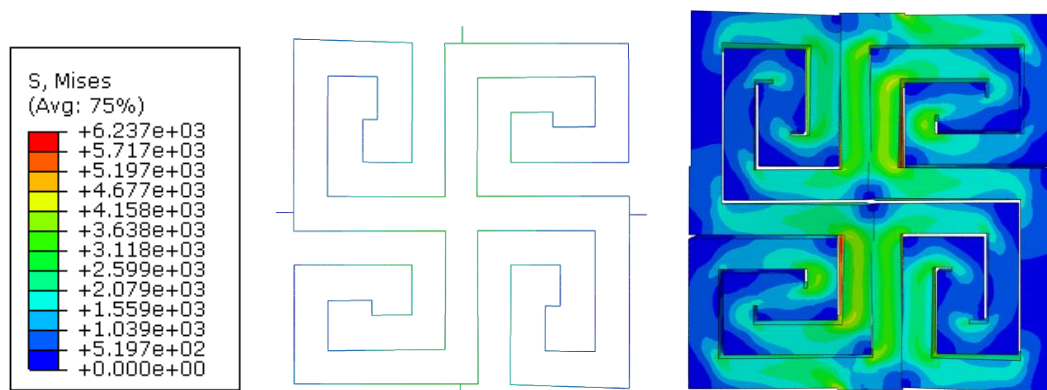
Figure III.11 Stress contour for beam and continuum models in case 3

44

Table III.4 Results for beam and continuum models in case 4

case4_bending				
continuum model		beam model		error value
force/lbf	displacement/inch	force/lbf	displacement/inch	
2.25E-06	5.20E-07			
2.25E-05	5.20E-06	1.12E-04	2.16E-05	
2.25E-04	5.20E-05	2.25E-04	4.33E-05	16.67%
2.25E-03	5.20E-04	2.25E-03	4.33E-04	16.67%
1.12E-02	2.60E-03	1.12E-02	2.16E-03	16.97%
2.25E-02	5.20E-03	2.25E-02	4.33E-03	16.67%
5.62E-02	1.30E-02	5.62E-02	1.08E-02	16.97%
1.12E-01	2.60E-02	1.12E-01	2.15E-02	17.25%
1.69E-01	3.91E-02	1.69E-01	3.23E-02	17.34%
2.25E-01	5.16E-02	2.25E-01	4.29E-02	16.79%
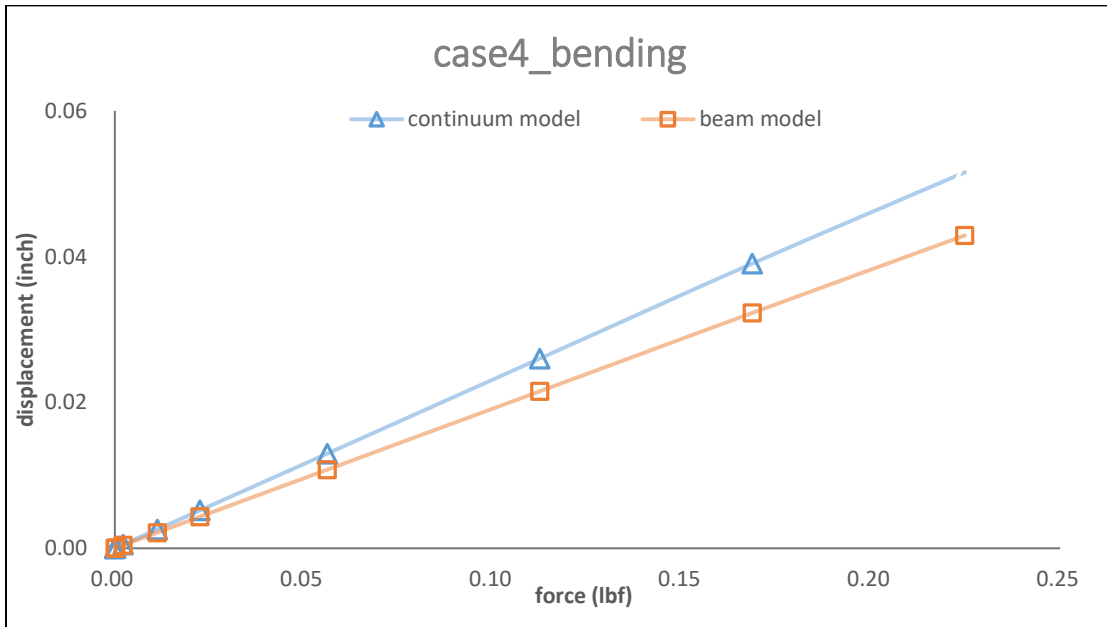
Figure III.12 The relation between displacement and force for beam and continuum models in case 4

3.2 Unit sections in different cutting density

In order to form desired geometrical shapes, the planar surface is required to have distinct flexibilities at different parts. Thus, three unit cells of the same pattern but with different cut densities are created in order to examine the effect of cut densities on overall deformations. These different patterns are named as dense_1, dense_2, dense_3 shown in Figure III.13 associated with the number of the cutline layers in a quarter unit-cell model. Dense_1 pattern has only one layer of cutline, while dense_2 and dense_3 patterns have 2 and 3 layers, respectively. All unit cells have the unit size of 1 inch x 1 inch and the thickness of 0.125 inches and the line shown on the cutline models is the actual size of the cutline.
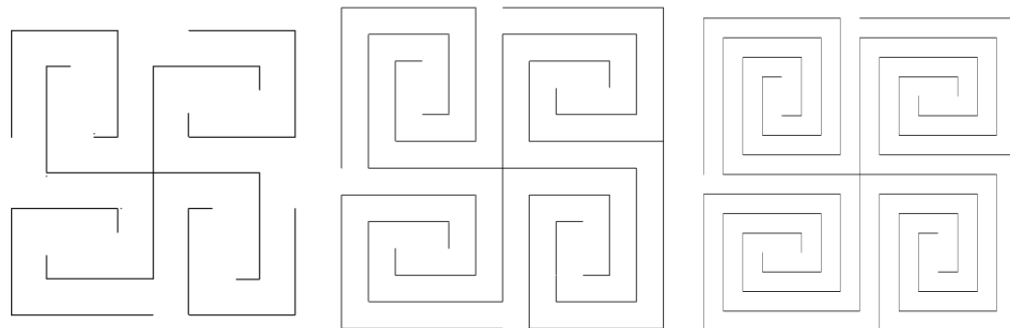
Cutline model (dense_1)   Cutline model (dense_2)   Cutline model (dense_3)

Figure III.13 Cutline model for dense_1, dense_2 and dense_3 unit sections

From the previous study on unit cells, the most fragile places are often the corners due to the stress concentration effect, so fillets (0.02 inch radius) are included to these models for all corners in order to improve their performance by avoiding failure at the junctions (sharp corner). Like the steps before, these patterns are simplified to beam

46

models in Figure III.14. All the models are meshed by linear beam element B31. According to the convergence study, the element sizes for dense_1 and dense_2 are both 0.003 inch and the element numbers are 2347 and 3691 respectively. For dense_3 model, the element size is 0.001 inch and the element number is 15114. The cross section area of the beams for these three models are shown in Table III.5. The following parametric study is to compare their flexibilities under same loading conditions.

beam_dense_1　　　　beam_dense_2　　　　beam_dense_3
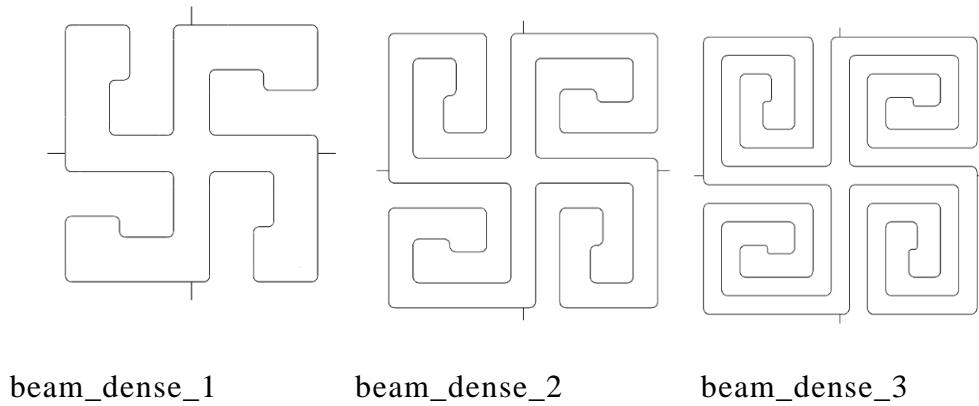
Figure III.14 Beam model for dense_1, dense_2 and dense_3 unit sections

Table III.5 Beam cross sections for three models

Beam cross section	Thickness(inch) x Width(inch)
Dense_1	0.1250 x 0.1000
Dense_2	0.1250 x 0.0583
Dense_3	0.1250 x 0.0375

3.2.1   Case 1 uniaxial extension

In uniaxial extension, the boundary condition is to constrain the top endpoint in all direction displacement and a displacement loading is applied at the bottom endpoint

along the vertical direction. The stress contour and displacement contour for these three unit sections under maximum loading are shown in Figure and Figure III.16, respectively. As expected the cut with higher density gives more flexible deformations due to a significantly low second moment of an area of each section between the cut lines. Adding more cut lines will certainly create more flexible structures. However, increasing cut lines leads to smaller area of each section between the cut lines, and hence reducing load carrying capability of the overall structures.

Figure III.15 Stress contour for dense_1, dense_2 and dense_3 unit sections in case 1

48

Figure III.15 Continued
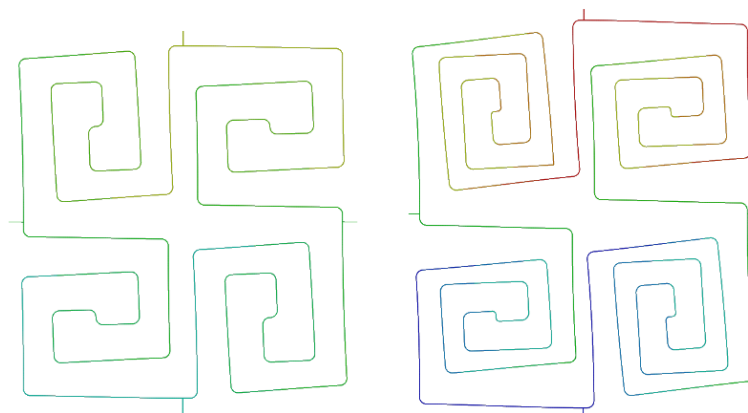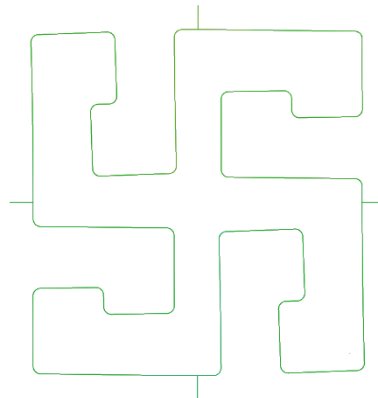
Figure III.16 Displacement contour for dense_1, dense_2 and dense_3 unit sections in case 1

49

3.2.2 Case 2 Twisting

In twisting, the boundary condition is to constrain the left and right endpoints in all direction displacement and concentrated loads are applied at the top and bottom endpoints in different out-plane directions. The stress contour and displacement contour for these three unit sections under maximum loading are shown in Figure   and Figure III.18, respectively. Similar observation like in the uniaxial case that higher density of cut lines leads to more flexible structures, due to reduction in the torsional rigidity of each section between the cut lines.
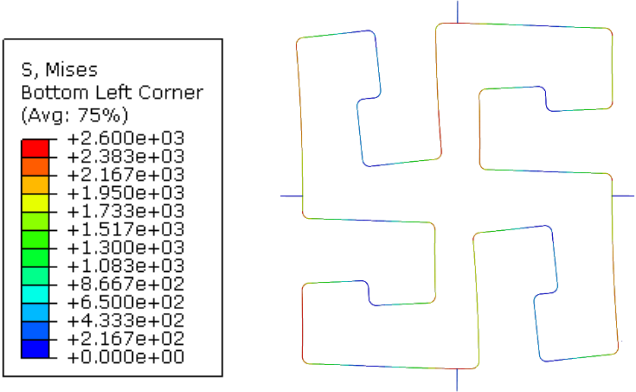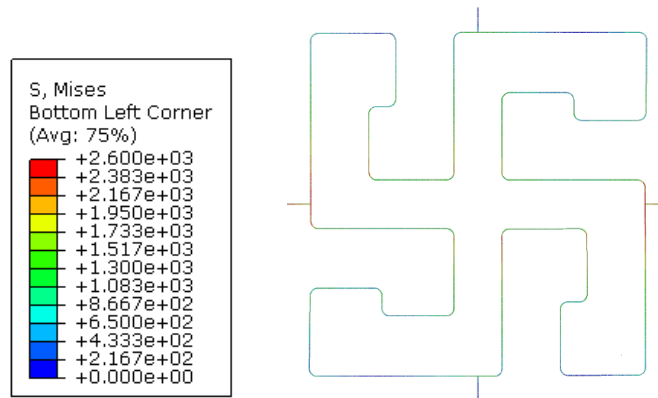

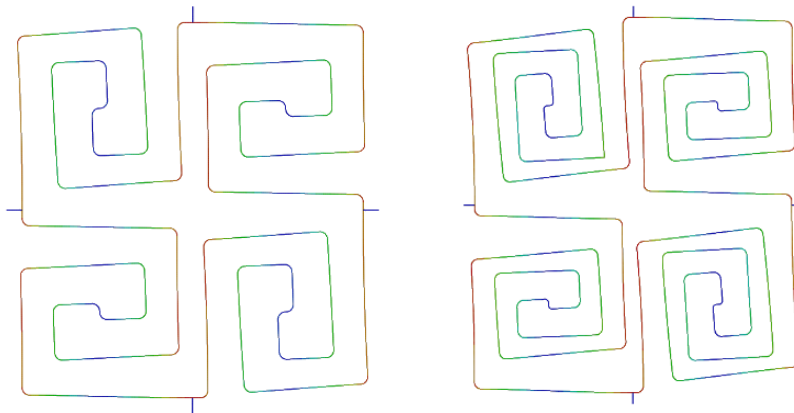**Figure III.17 Stress contour for dense_1, dense_2 and dense_3 unit sections in case 2**
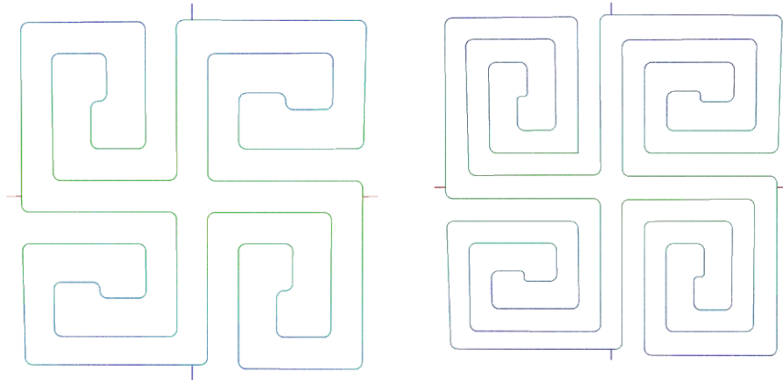
Figure III.17 Continued
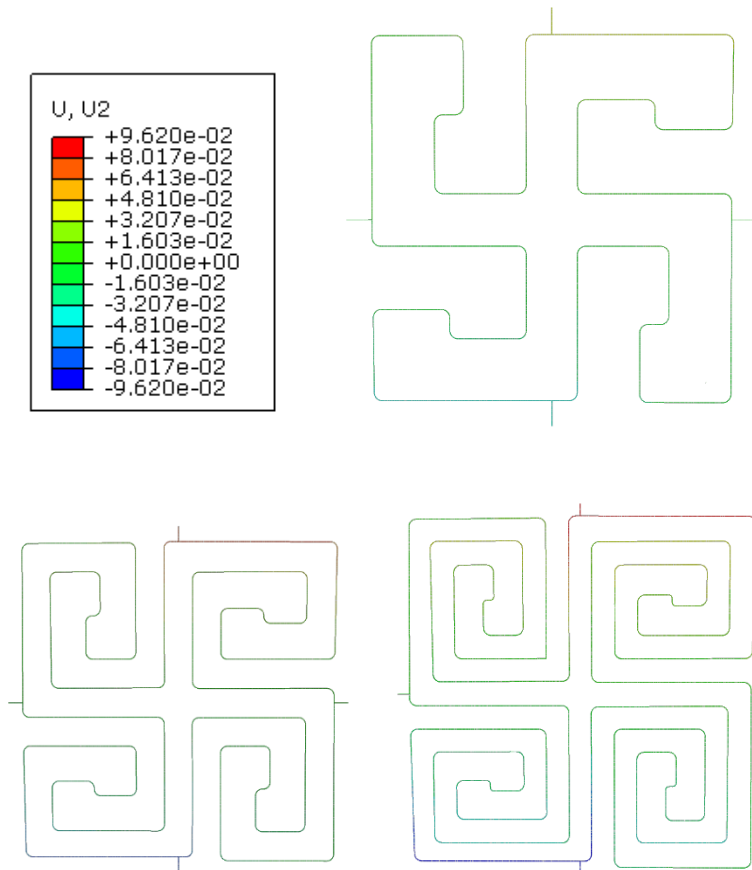
Figure III.18 Displacement contour for dense_1, dense_2 and dense_3 unit sections in case 2

51

3.2.3   Case 3 Bending

In bending, the boundary condition is to constrain the left and right endpoints in all direction displacement and concentrated loads are applied at the top and bottom endpoints in the same out-plane direction. The stress contour and displacement contour for these three unit sections under maximum loading are shown in Figure III.19 and Figure III.20, respectively.
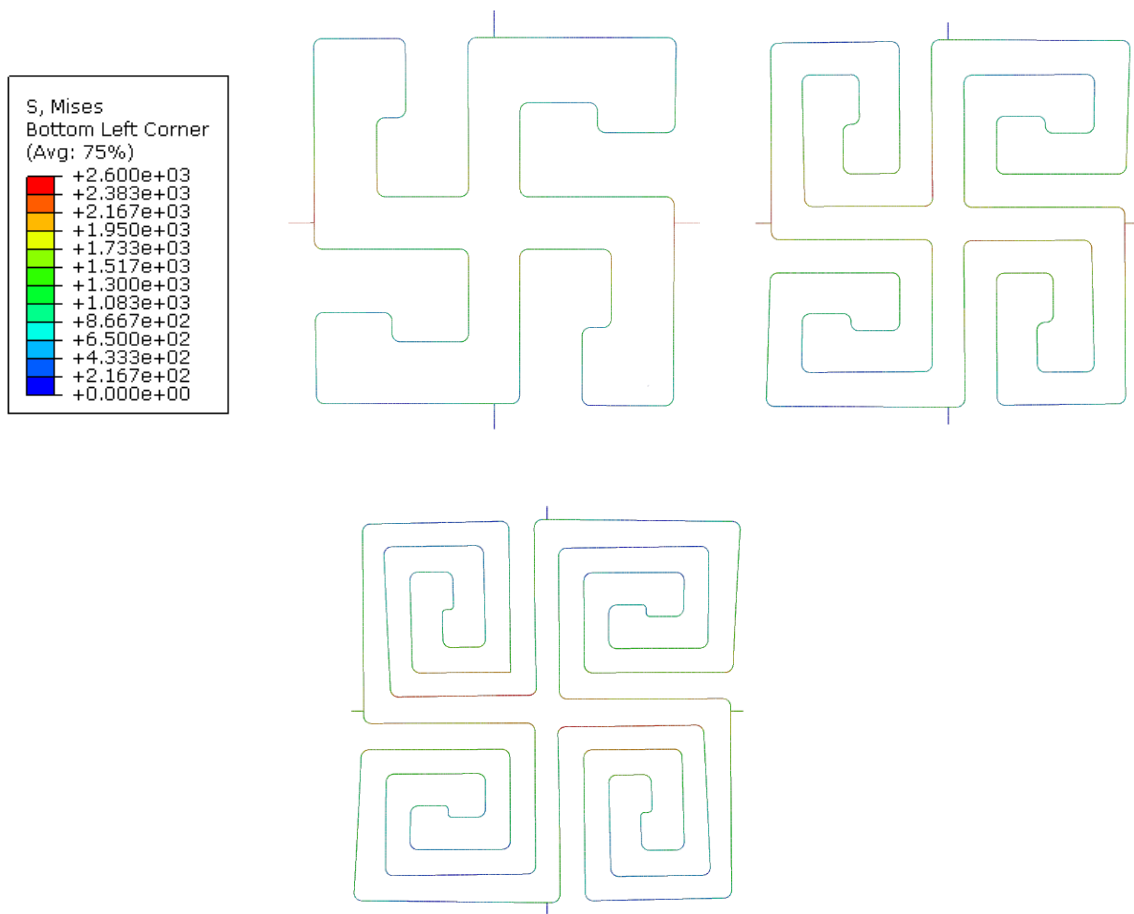
Figure III.19 Stress contour for dense_1, dense_2 and dense_3 unit sections in case 3

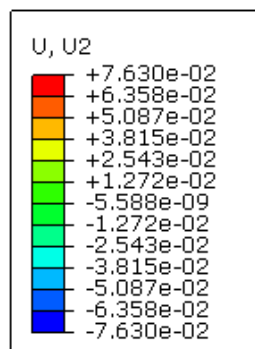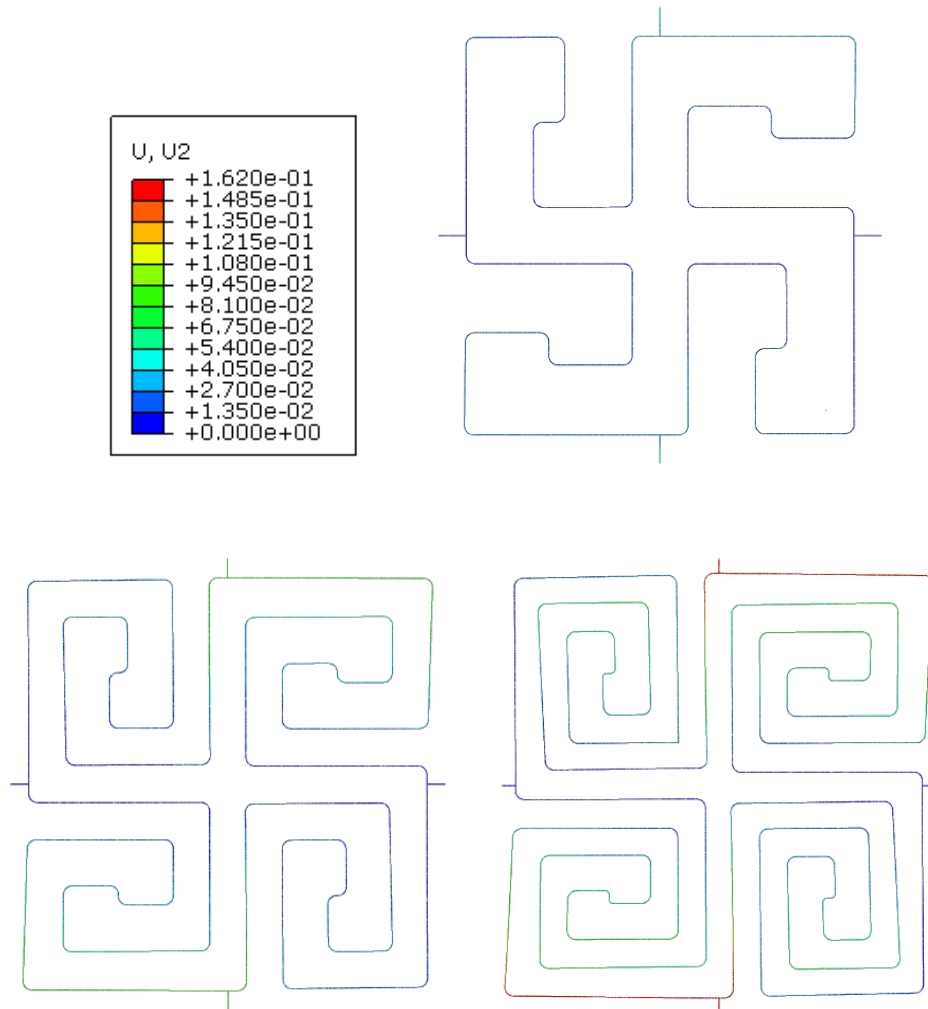**Figure III.20 Displacement contour for dense_1, dense_2 and dense_3 unit sections in case 3**

According to the data collected in the results,we can get Table III.6 to compare the responses of different patterns under different loading cases. The maxium loads for three unit sections in the cases are shown in Table III.7. These maximum values for the displacements and loads are determined based on the maximum stresses in the section, which is constraint to the failure stress of the MDF (2.6x103 psi).

Table III.6 Maximum displacement for dense_1, dense_2 and dense_3 unit sections in three cases

Maximum Displacement(inch)	Dense_1	Dense_2	Dense_3
Uniaxial extension	1.390e-2	3.707e-02	7.627e-02
Bending	3.795e-2	9.332e-02	1.622e-01
Twisting	4.277e-2	7.149e-02	9.608e-02

Table III.7 The maximum force for dense_1, dense_2 and dense_3 unit sections in three cases

Maximum force(lbf)	Dense_1	Dense_2	Dense_3
Uniaxial extension	4.5	1.45	0.60
Bending	2.5	1.35	0.40
Twisting	2.5	0.90	0.35
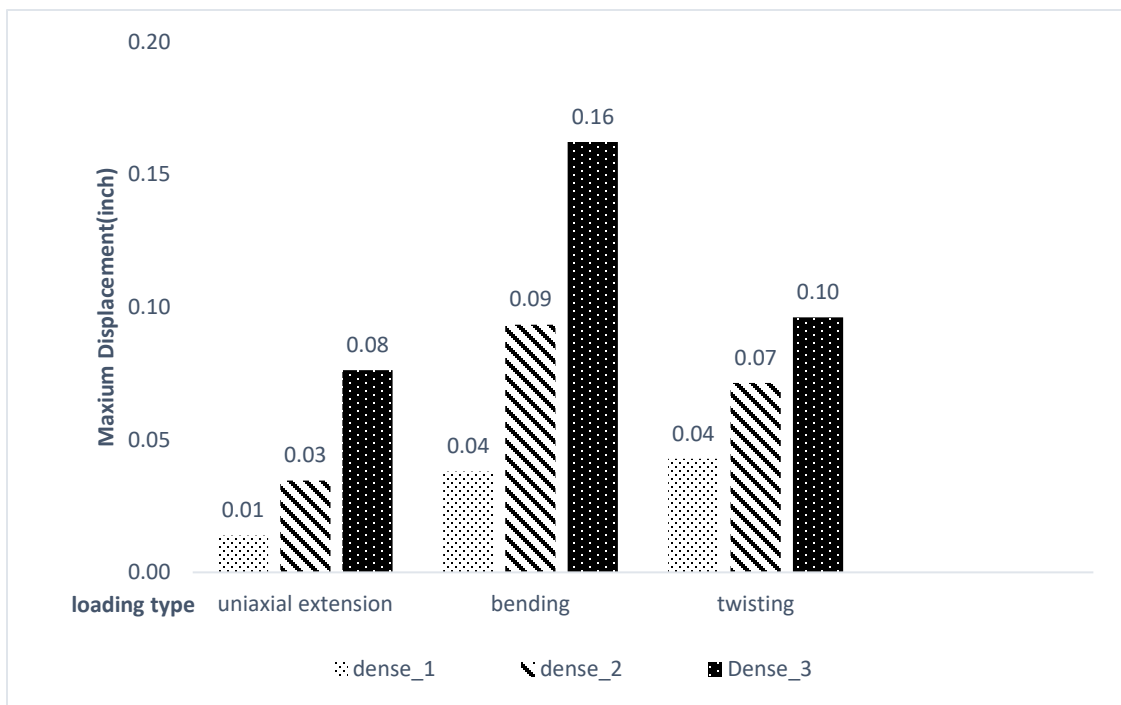
Figure III.21 Maximum displacement for dense_1, dense_2 and dense_3 unit sections in three cases
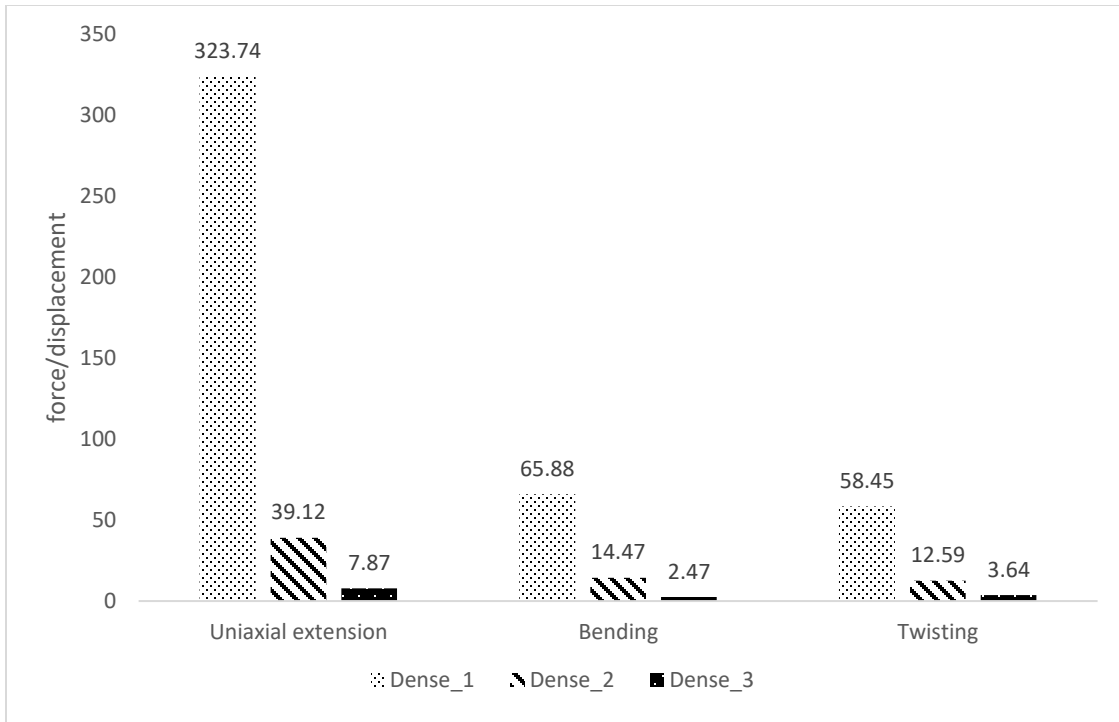
Figure III.22 The relation between force and displacement for dense_1, dense_2 and dense_3 unit sections in three cases

From Figure III.21, higher cutting densities in the unit cells will result in more flexiblities and this characteristics is more obvious under uniaxial extension and bending conditions. However it results in low load carrying capability of the structures. The relations between force and displacement are taken as the rigidities for the unit sections shown in Figure III.22. The unit sections with less cutting shows larger rigidities in all cases.

3.3 Experiments

With the further study on these unit cells, experiments are done on these unit cells by prescribing axial deformation to the unit-cells in contrast to the simulation results.

The experiments were done at Dr. Michael Moreno's lab at Texas A&M University.

3.3.1   *Uniaxial extension*

Before the experiment, the sizes of the specimen handles are measured for the documentations. The sample is installed between two grips shown in Figure III.23 and the cramp marking lines are made to figure out there is no slip between the sample and grips during experiment. After the installation of the specimen, data acquire interval, the strain and the strain rate are set for the case. By slightly adjustment for the initial load and initial stroke, the grip distance is measured to work out the actual displacement and speed for each case. Then the experimental set-up is completed. During the uniaxial extension experiment, the grip_1 holds one side of the specimen statically, while the grip_2 stretch the specimen along the certain axis at the constant speed. Meanwhile, the forces and displacement are captured every interval set previously. We have three kinds of samples tested at two different strain rates (1% and 0.1%). The relation between the reaction forces and displacements for these three unit sections are plotted in Figure III.24.

Figure III.23 The experiment instrument
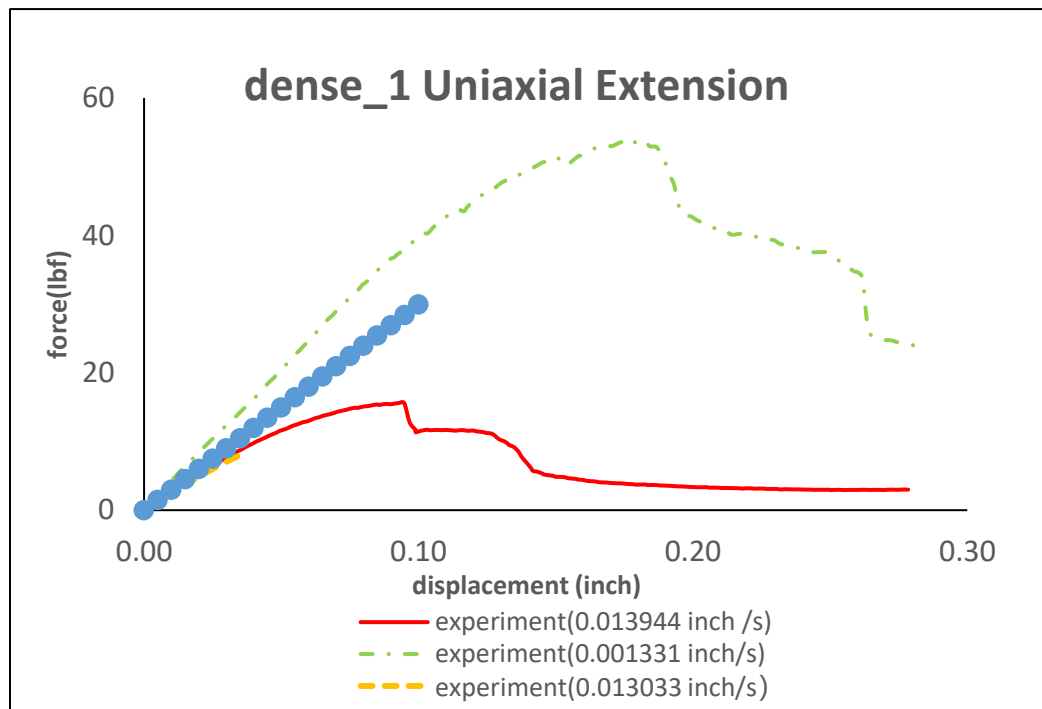
Figure III.24 Experiment data and simulation results for dense_1, dense_2 and dense_3 in uniaxial extension

dense_2 Uniaxial Extension

dense_3 Uniaxial Extension
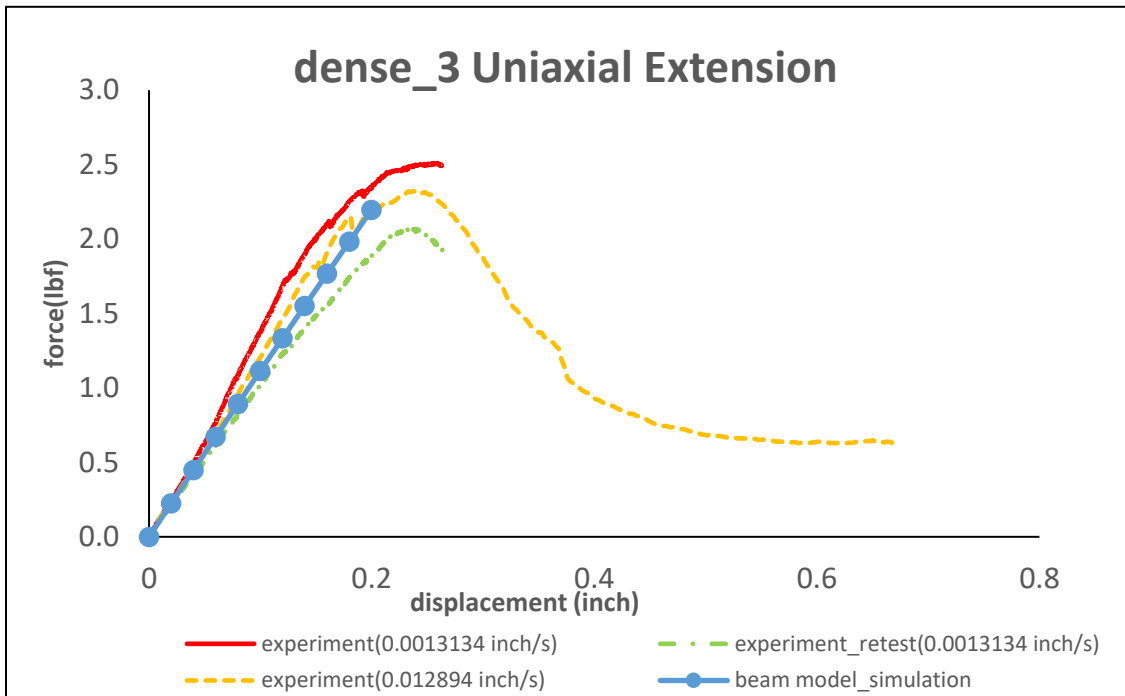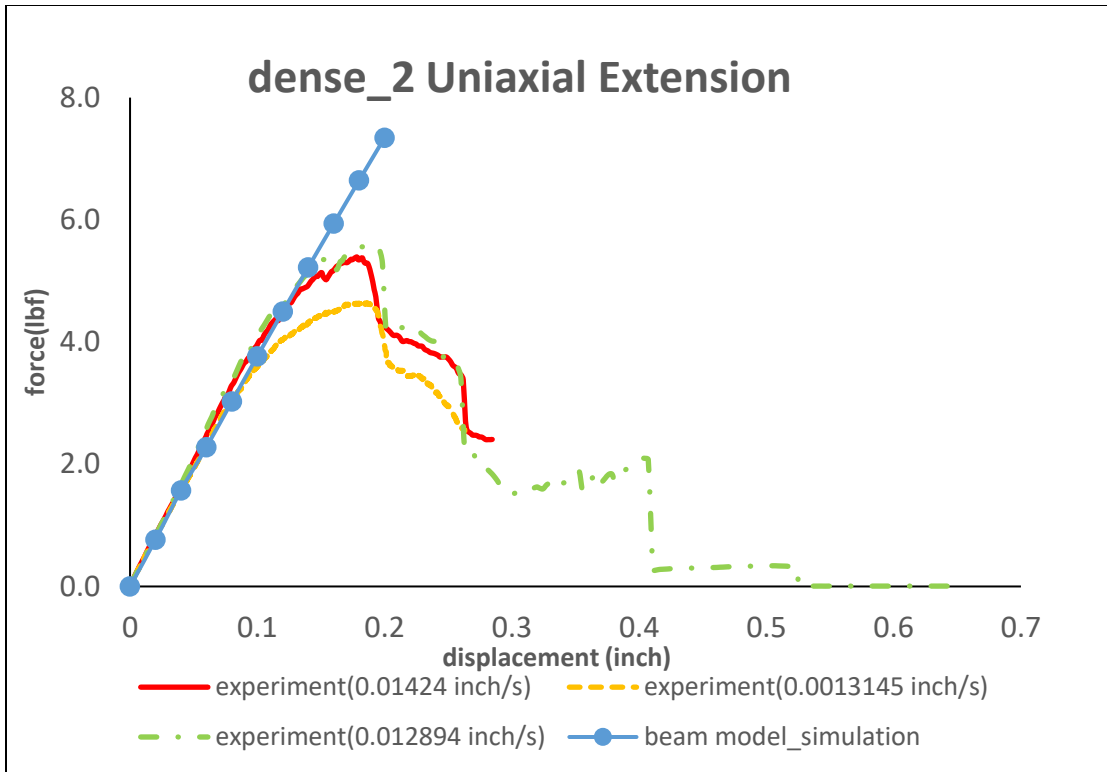
Figure III.24 Continued

These figures are in large displacements and they show some nonlinearity in material properties when failure starts. In order to discuss the linear behavior of these unit section which is used in simulation results, the parts of the displacements below 0.05 inch are considered. In this way, the experiment data can be assumed approximately linear. From Figure III.25, the experimental data match the simulation quite well and the experiment rates do not affect the results much. However, in dense_1 uniaxial case, the relative slow rate experiment in redline shows considerable differences with other results.
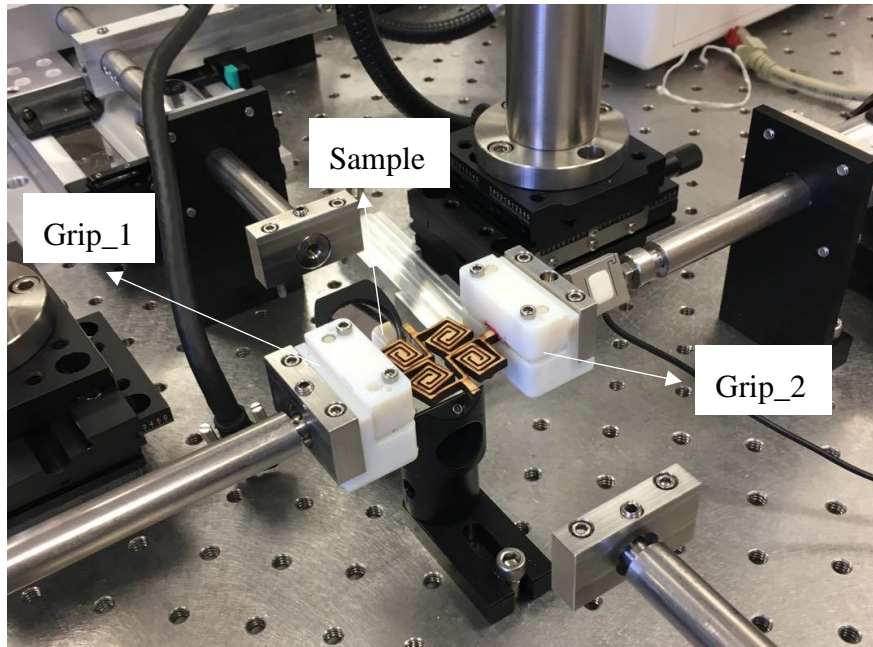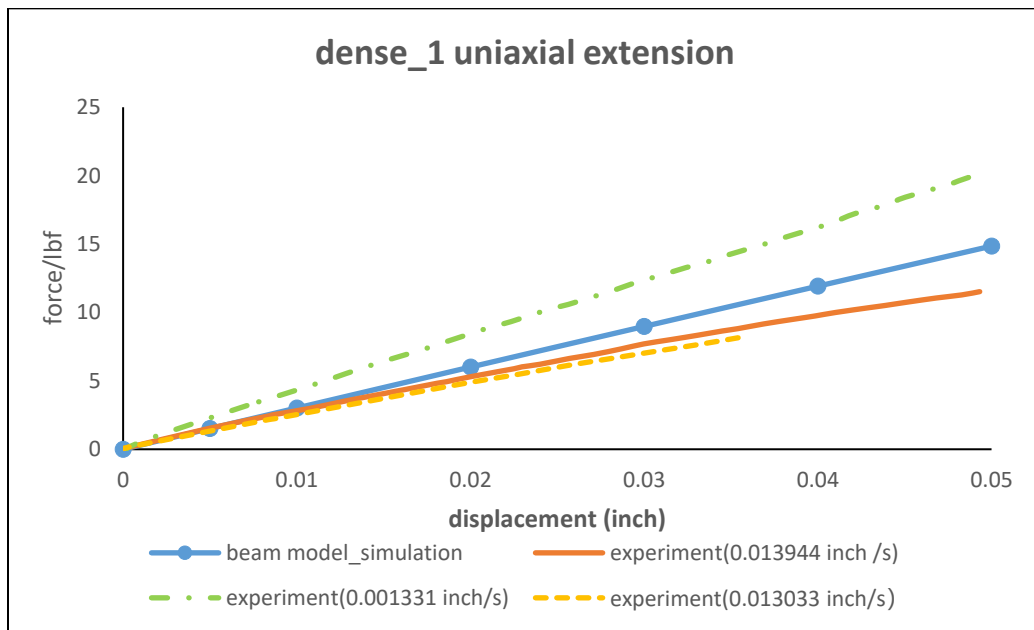

Figure III.25 Experiment data and simulation results for dense_1, dense_2 and dense_3 in uniaxial extension under 5% strain

dense_2 uniaxial extension

dense_3 uniaxial extension
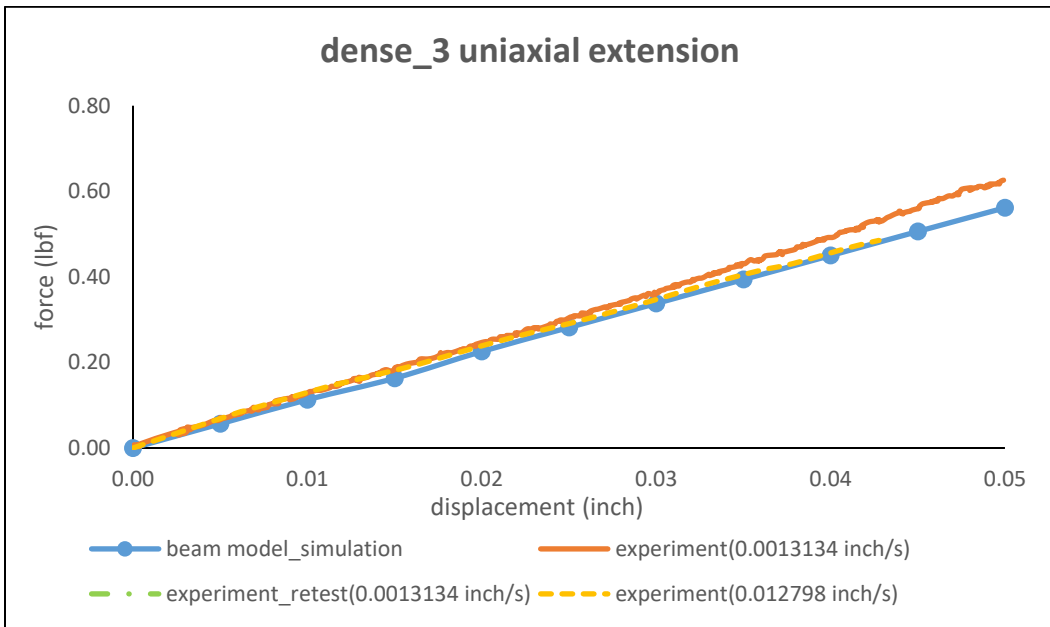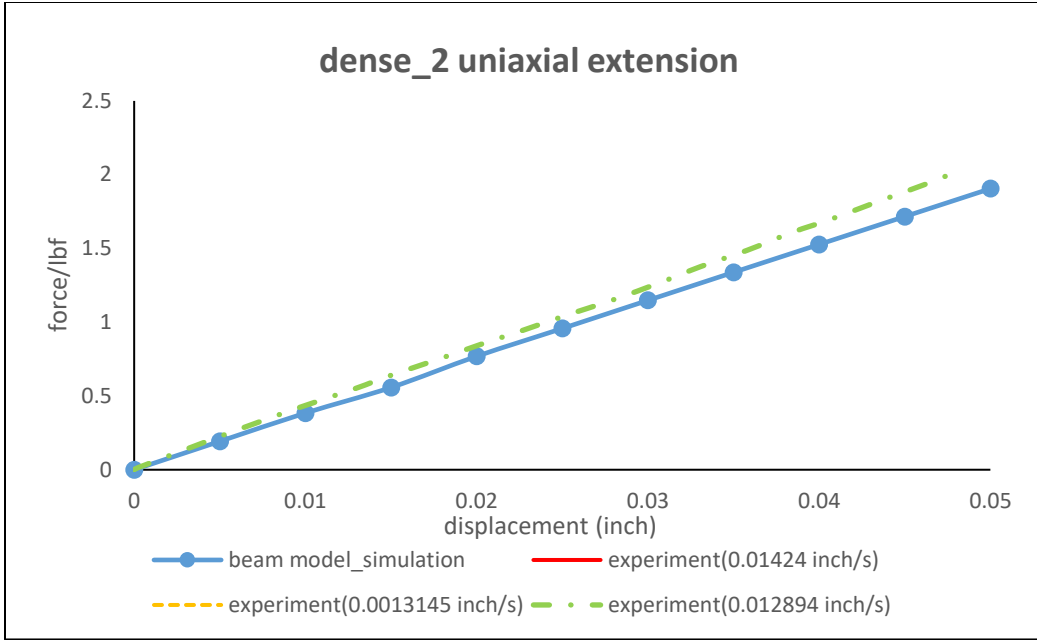
Figure III.25 Continued

3.4 Applications

3.4.1 Dome shape

After the study on the unit cells, we create a large panel with varying cut densities in order to achieve a desired deformed shape. A 15 inch x 15 inch panel is initially designed in Figure III.26. The goal is to generate a dome shape deformation.

The center area in yellow is 7 inchx7 inch of dense_3 patterns to make the center part of the panel most soft, which is surrounded by 2 inches of dense_2 patterns in grey on each side. The edge of the panel in blue consists of 2-inches dense_1 patterns.
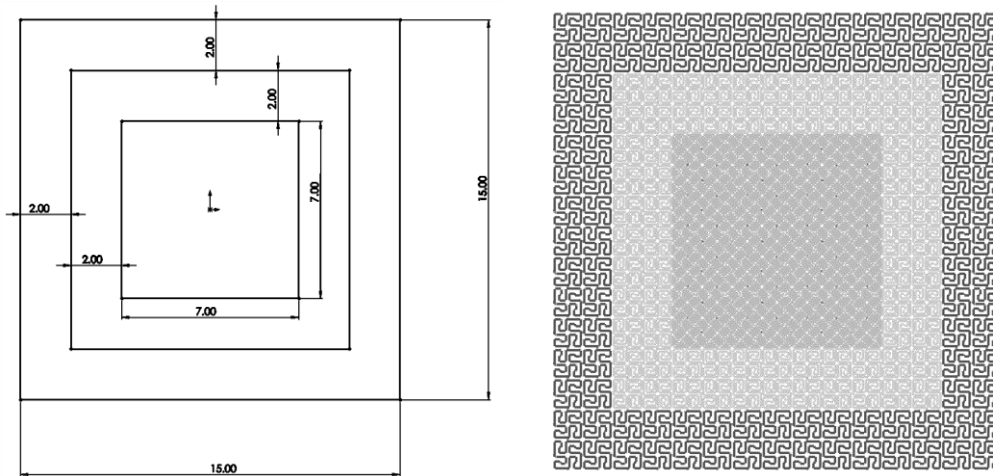
Figure III.26 The panel model for the dome shape

For the large panel, how to deal with the connection between two distinct unit sections should be taken into consideration. The connection does not have the same length magnitude as the main part of unit cells. Also, in actual situations, the connection part is a rectangular rather than a square from front view, like the shade area in Figure III.27. This is the connection example between dense_2 and dense_3.
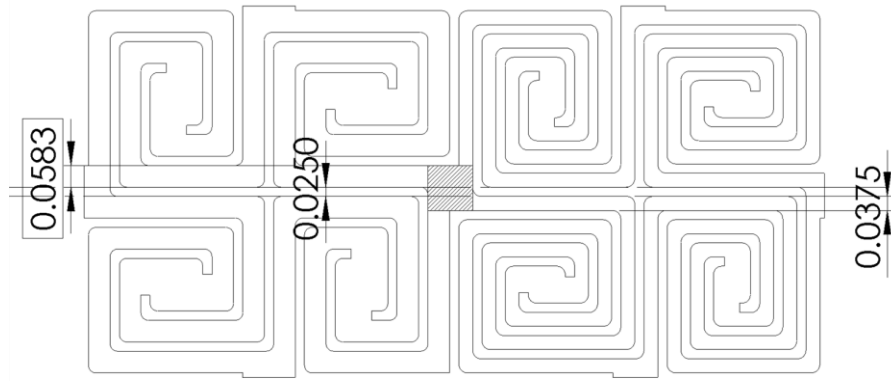
Figure III.27 The connection example between dense_2 and dense_3

As shown in Figure III.27, the width of the connection part is made up of three parts, the width of the beam for the left pattern, the width of the beam for the right pattern and the gap distance of laser cutting. However, if the left and right patterns are not the same, the connection will not be symmetric along the centerline. The problem is that, for the simplified beam models, in order to make the connections possible, we have to set the connection beams along the centerline of each unit sections (dense_2 beam model and dense_3 beam model) like in Figure III.28.
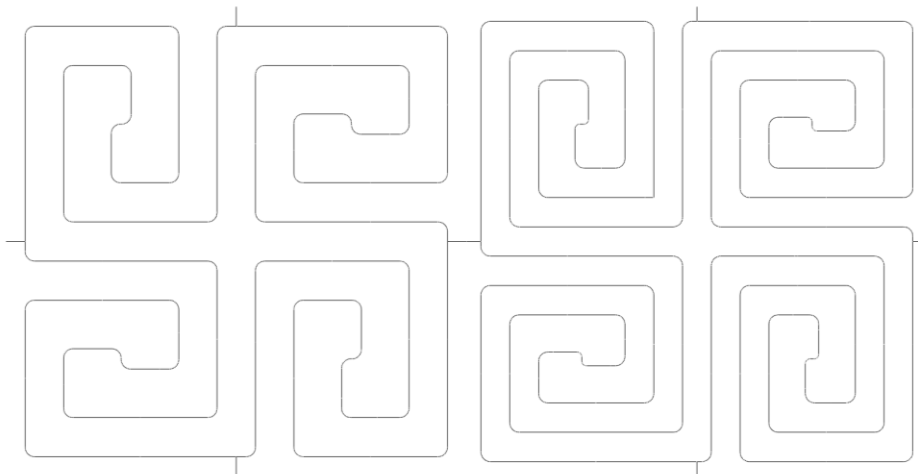
Figure III.28 The connection of the beam models between dense_2 and dense_3

In this way, we need to assume that the connection part should be simplified to be symmetric for beam models. The simplification is to choose the smaller beam width value (like 0.0375 inch shown above) to replace of the larger beam width value (like 0.0583 inch shown above). Thus, the width of the connection part should be set as 0.1 (0.0375+0.0250+0.03750) inch instead of the original 0.1208 (0.0583+0.0250+0.03750) inch.

According to the discussion above, there should be 8 different rectangular cross sections for the unit sections in the panel and the thickness for all unit section is 0.125 inch.

Table III.8 The parameters for beam cross sections

Beam cross section	Thickness(inch) x Width(inch)
Dense_1	0.1250 inch x 0.1000 inch
Dense_2	0.1250 inch x 0.0583 inch
Dense_3	0.1250 inch x 0.0375 inch
Connections between dense_1 pattern and dense_1 pattern	0.1250 inch x 0.2250 inch
Connections between dense_2 pattern and dense_2 pattern	0.1250 inch x 0.1417 inch
Connections between dense_3 pattern and dense_3 pattern	0.1250 inch x 0.1000 inch
Connections between dense_1 pattern and dense_2 pattern	0.1250 inch x 0.1417 inch
Connections between dense_2 pattern and dense_3 pattern	0.1250 inch x 0.1000 inch

With the model created, the boundary condition for the case is to constrain the four edges in the displacement of all directions and apply pressure on the center part of the panel. The element type and size is used as discussed previously. The analysis was performed until the maximum stress in the panel reaches the material tensile strength (2.6×10^3 psi) and the stress contour under maximum loading is shown in Figure III.29.

From the deformed shape in Figure III.30, it is like a dome with the center deformed much more than the surroundings. It does turn the stiff surface into a more flexible one with the help of cutting.

S, Mises
Bottom Left Corner
(Avg: 75%)
```
+2.600e+03
+2.383e+03
+2.167e+03
+1.950e+03
+1.733e+03
+1.517e+03
+1.300e+03
+1.083e+03
+8.667e+02
+6.500e+02
+4.333e+02
+2.167e+02
+0.000e+00
```
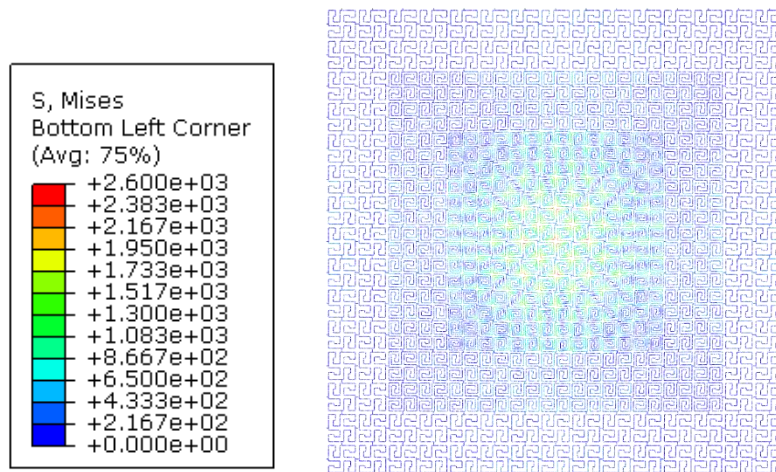
Figure III.29 Stress contour for the dome shape panel
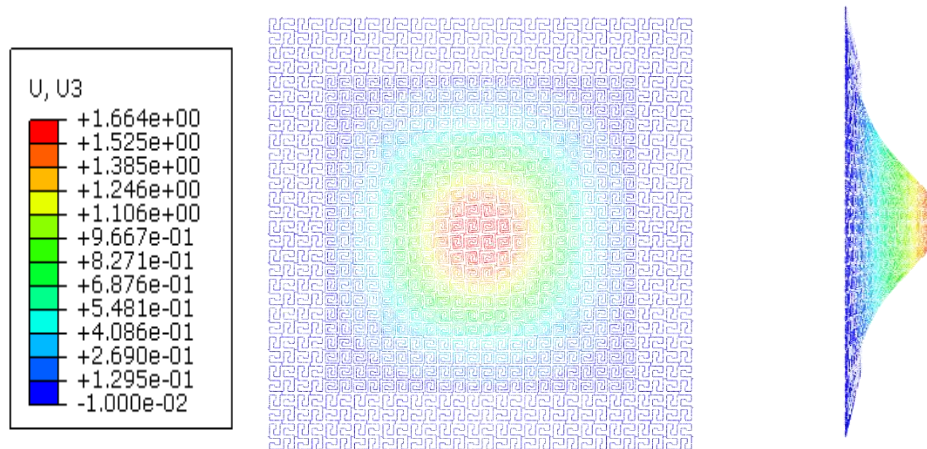
Figure III.30 Displacement contour for the dome shape panel

3.4.2 Saddle shape

For more applications, we want to acquire the desired deformed shape using certain arrangements of these unit cells with different densities. A saddle roof is a quite popular shape in architecture buildings and it is actually a paraboloid which require large flexibilities of the structures. In this work, we want to form a saddle shape like the surface z = 2xy.
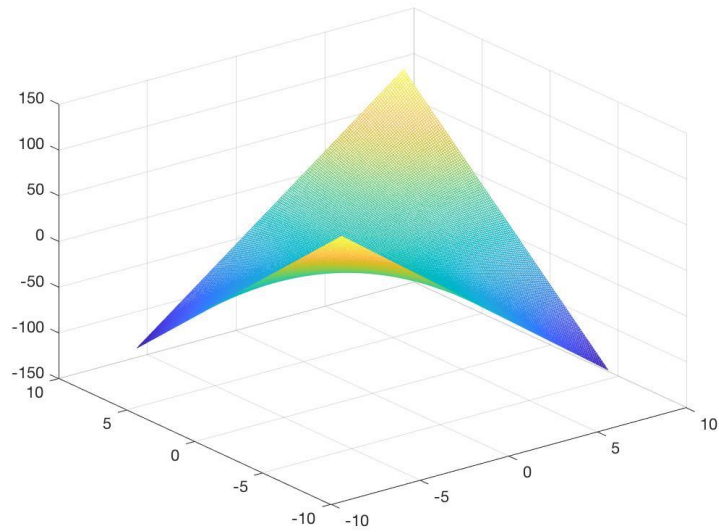
Figure III.31 The surface z = 2xy

A 15x15 inch panel as well as the three different unit sections are still used and the original point is located in the center point of the pane. The basic result we get from the previous works is that more cuttings account for more flexibilities among these patterns, so higher dense patterns are located in the locations with larger curvatures.

K1 is used for the slope of trace of the function f(x, y) for y=b (b is a constant) along with the x-axis and K2 is for the slope of trace of the function f(x, y) for x=a (a is a constant) along with the y-axis. T is used as the total curvature for x and y axes. The expression is shown in Equation (III.1).

$$K1 = \frac{\partial z}{\partial x} \; ; \; K2 = \frac{\partial z}{\partial y} \; ; \; T = K1^2 + K2^2 \qquad (III.1)$$

In the panel, there are 225 unit sections and due to three different patterns we have, they are divided into three groups based on the T of the center point of each unit section. The first group includes the parts whose T are larger than 50 and locations in this group

will be taken place by dense_3 patterns. The second group is those locations with T less than 10 and dense_1 patterns will be placed there. The rest are occupied by dense_2 patterns.

98	85	74	65	58	53	50	49	50	53	58	65	74	85	98
85	72	61	52	45	40	37	36	37	40	45	52	61	72	85
74	61	50	41	34	29	26	25	26	29	34	41	50	61	74
65	52	41	32	25	20	17	16	17	20	25	32	41	52	65
58	45	34	25	18	13	10	9	10	13	18	25	34	45	58
53	40	29	20	13	8	5	4	5	8	13	20	29	40	53
50	37	26	17	10	5	2	1	2	5	10	17	26	37	50
49	36	25	16	9	4	1	0	1	4	9	16	25	36	49
50	37	26	17	10	5	2	1	2	5	10	17	26	37	50
53	40	29	20	13	8	5	4	5	8	13	20	29	40	53
58	45	34	25	18	13	10	9	10	13	18	25	34	45	58
65	52	41	32	25	20	17	16	17	20	25	32	41	52	65
74	61	50	41	34	29	26	25	26	29	34	41	50	61	74
85	72	61	52	45	40	37	36	37	40	45	52	61	72	85
98	85	74	65	58	53	50	49	50	53	58	65	74	85	98

Dense_1
Dense_2
Dense_3

Figure III.32 The arrangement for three different unit sections

As Figure III.32 shown, each grid stands for a unit section and the number in the grids are the T of the center point of each grid. Also, yellow, red and green are the symbols of group 1, 2 and 3, respectively. Considering the connection of the unit sections, a new beam panel is created in Figure III.33. The model is meshed as discussed before.
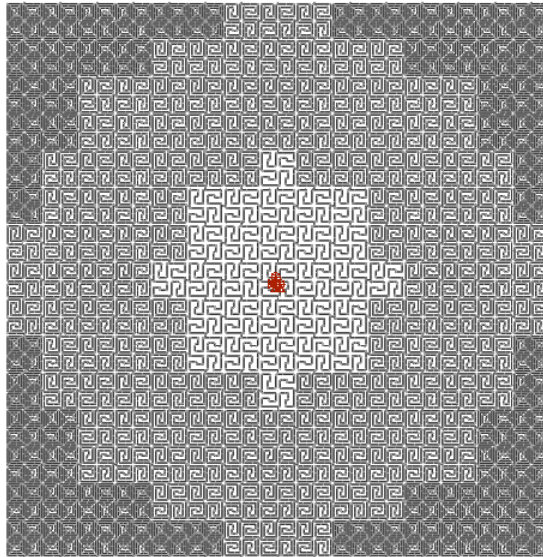
Figure III.33 The panel model for the saddle shape

In order to form the saddle shape, we apply out-plane forces on two corners on the same diagonal and opposite direction pressure on the rest two corners. The boundary condition is to constrain three points in the center of the panel shown as the orange region in Figure III.33 in the way discussed previously to eliminate the rigid body motion. Similiarly, we keep the stress limitation as the material tensile strength (2.6E3 psi) and the stress contour and the deformed shape under maximum loading are shown in Figure III.34 and Figure III.25.

Stress contour in undeformed shape (psi)

Figure III.34 Stress contour for the saddle shape panel

Displacement contour in undeformed shape and deforemed shape (inch)

Figure III.35 Displacement contour for the saddle shape panel

Figure III.35 Continued

CHAPTER IV

CONCLUSIONS AND FUTURE WORKS

This study has presented numerical analyses of large deformations in flexible structures subjected to thermal and mechanical stimuli. Two flexible systems have been studied. The first system is made of bil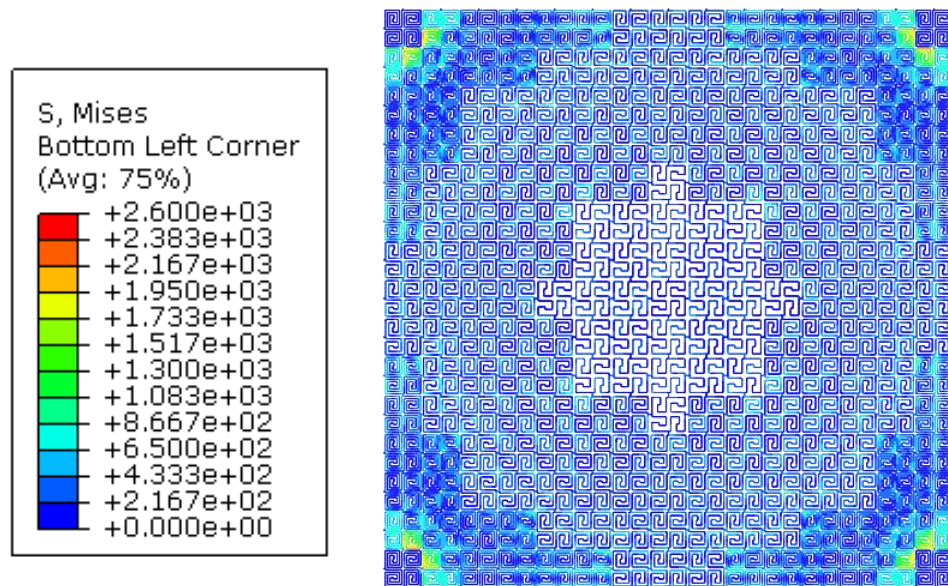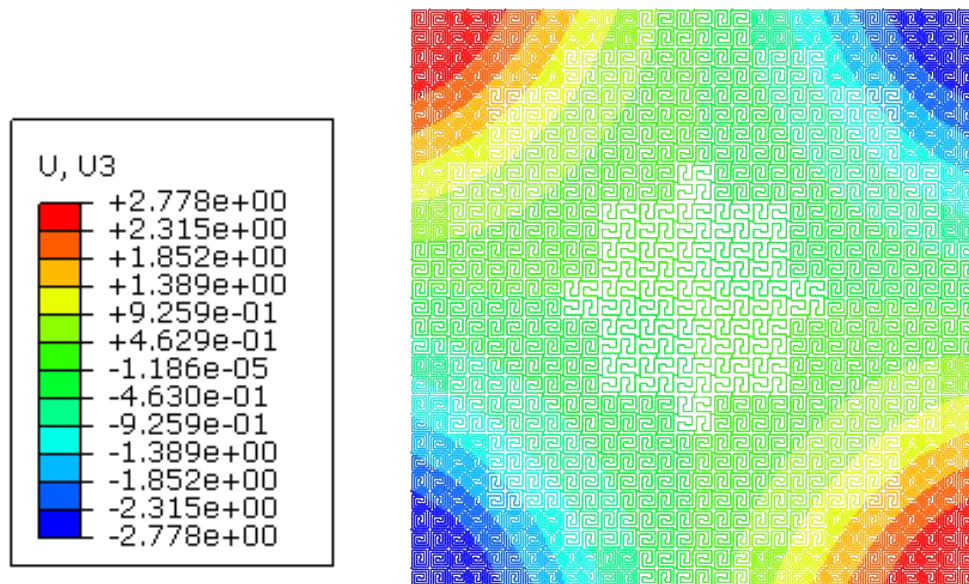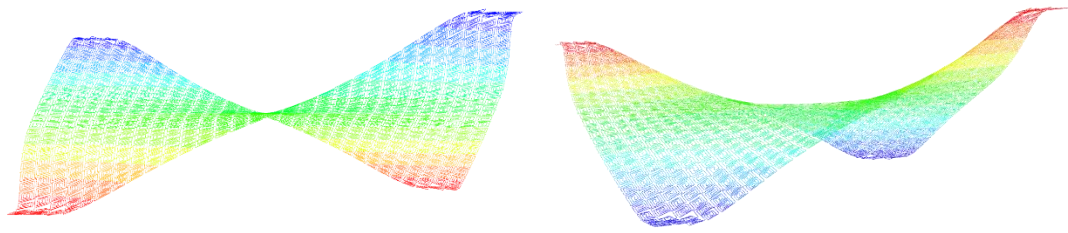ayers having different material properties for each layer. The bilayers are subjected to temperature changes and the deformed shapes are examined. Parametric studies have been conducted on the bilayers in order to understand the effects of several material and geometrical parameters on the overall deformations of the bilayers. Examples are illustrated to show the applications of the thermal actuation of the thin layer structures. In this study, only constant temperature change is considered. In the future, one can consider a coupled heat conduction and deformation in the bilayers, so that evolutions of the deformed shapes due to time-dependent changes in the temperature field can be incorporated.

The second system consider a flexible structure due to kerfing. One kerfing pattern, i.e., interlocked Archimedean spiral, has been considered. Parametric studies are conducted in order to understand the effect of cut densities and loading conditions on the overall deformations of the kerf patterns. As expected kerfing with higher cut densities leads to more flexible deformations, but reduces the load carrying capabilities of the structures. Two examples of flexible structures with different kerfing configurations are shown to illustrate how to form desired shapes by arranging the repeated unit sections of the kerfing patterns with different cut densities. In this work, only one specific pattern have been studied and considered for the entire panel. There are a great variety of cutting patterns having different performance in deformations. So

including several kinds of patterns in a panel can be considered in order to achieve various desired complex shapes.

REFERENCES

[1] Otsuka, K. and Wayman, C.M. eds., 1999. Shape memory materials. Cambridge university press.

[2] Liu, Y., Liu, L., Zhang, Z., Jiao, Y., Sun, S. and Leng, J., 2010. Analysis and manufacture of an energy harvester based on a Mooney-Rivlin–type dielectric elastomer. EPL (Europhysics Letters), 90(3), p.36004.

[3] Li, B., Liu, L. and Suo, Z., 2011. Extension limit, polarization saturation, and snap-through instability of dielectric elastomers. International Journal of Smart and Nano Materials, 2(2), pp.59-67.

[4] Suo, Z., 2010. Theory of dielectric elastomers. Acta Mechanica Solida Sinica, 23(6), pp.549-578.

[5] Gunes, I.S. and Jana, S.C., 2008. Shape memory polymers and their nanocomposites: a review of science and technology of new multifunctional materials. Journal of Nanoscience and Nanotechnology, 8(4), pp.1616-1637.

[6] Meng, Q. and Hu, J., 2008. Self-organizing alignment of carbon nanotube in shape memory segmented fiber prepared by in situ polymerization and melt spinning. Composites Part A: Applied Science and Manufacturing, 39(2), pp.314-321.

[7] Yu, K., Liu, Y. and Leng, J., 2011. Conductive shape memory polymer composite incorporated with hybrid fillers: electrical, mechanical, and shape memory properties. Journal of Intelligent Material Systems and Structures, 22(4), pp.369-379.

[8] Tandon, G.P., Goecke, K., Cable, K. and Baur, J., 2010. Environmental durability of fabric-reinforced shape-memory polymer composites. Journal of Intelligent Material Systems and Structures, 21(14), pp.1365-1381.

[9] Bar-Cohen, Y., Bao, X., Sherrit, S. and Lih, S.S., 2002. Characterization of the electromechanical properties of ionomeric polymer-metal composite (IPMC).

[10]   Samatham, R., Kim, K., Dogruer, D., Choi, H., Konyo, M., Madden, J.Nakabo, Y., Nam, J., Su, J., Tadokoro, S., Yim, W., Yamakita, M., 2007.Active polymers: An overview. In: Kwang, K.J., Tadokoro, S. (Eds.), Electroactive Polymers for Robotic Applications. Springer, chapter 1.

[11]   Kornbluh, R., Pelrine, R., Eckerle, J. and Joseph, J., 1998, May. Electrostrictive polymer artificial muscle actuators. In Robotics and Automation, 1998. Proceedings. 1998 IEEE International Conference on (Vol. 3, pp. 2147-2154). IEEE.

[12]   Tajeddini, V. and Muliana, A., 2017. Deformations of flexible and foldable electro-active composite structures. Composite Structures, 160, pp.280-291.

[13]   Ask A, Menzel A, Ristinmaa M. On the modelling of electro-viscoelastic response of electrostrictive polyurethane elastomers. InIOP Conference Series: Materials Science and Engineering 2010 (Vol. 10, No. 1, p. 012101). IOP Publishing.

[14]   Ask, A., Menzel, A. and Ristinmaa, M., 2012. Phenomenological modeling of viscous electrostrictive polymers. International Journal of Non-Linear Mechanics, 47(2), pp.156-165.

[15]   Ask, A., Menzel, A. and Ristinmaa, M., 2012. Electrostriction in electro-viscoelastic polymers. Mechanics of Materials, 50, pp.9-21.

[16]   Boley, B.A. and Weiner, J.H., 2012. Theory of thermal stresses. Courier Corporation.

[17]   Boley, B.A. and Testa, R.B., 1969. Thermal stresses in composite

beams. International Journal of Solids and Structures, 5(10), pp.1153-1169.

[18]   Horvay, G. and Born, J.S., 1953. THERMAL STRESSES IN RECTANGULAR

STRIPS. PART 1 (No. KAPL-1001). Knolls Atomic Power Lab.

[19]   Durelli, A.J. and Tsao, C.H., 1955. Determination of Thermal Stresses in

Three-Ply Laminates. Journal of Applied Mechanics, 77, pp.190-192.

[20]   Eischen, J.W. and Everett, J.S., 1989. Thermal stress analysis of a bimaterial

strip subject to an axial temperature gradient. Journal of Electronic Packaging, 111(4),

pp.282-288.

[21]   Khan, K.A., 2011. A multiscale model for coupled heat conduction and

deformations of viscoelastic composites. Texas A&M University.

[22]   Jeon, J., 2013. A Viscoelastic-Viscoplastic Analysis of Fiber Reinforced

Polymer Composites Undergoing Mechanical Loading and Temperature

Changes (Doctoral dissertation).

[23]   Zhang, Z., Ye, G., Wu, H., Wu, H., Chen, D. and Chai, G., 2015. Thermal

effect and active control on bistable behaviour of anti-symmetric composite shells

with temperature-dependent properties. Composite Structures, 124, pp.263-271.

[24]   Bartels S, Bonito A, Muliana A, Nochetto R, "Modeling and Simulation of

Thermally Actuated Bilayer Plates," Journal of Computational Physics, 354, pp. 512-

528, 2018

[25]   Hoffer, B., 2016. Kerf Pavilion. [Sl]: IAP Pavilion Competition, 2012. Acesso

em, 15.

[26]   D. Ivani˘sevi´c, 2014. Super flexible laser cut plywood:

lab.kofaktor.hr/en/portfolio/super-flexible-laser-cut-plywood/

[27]   Zarrinmehr, S., Ettehad, M., Kalantar, N., Borhani, A., Sueda, S. and Akleman, E., 2017. Interlocked archimedean spirals for conversion of planar rigid panels into locally flexible panels with stiffness control. Computers & Graphics.

[28]   Guzelci, O., Alaçam, S. and Bacınoğlu, S. (2018), Three-step experimentation on embedding curvature to rigid planar materials through cut patterns.

[29]   Greenberg, E. and Körner, A., 2014. Subtractive Manufacturing for Variable-Stiffness Plywood Composite Structures. Sustainable Design and Manufacturing.

[30]   Muliana, Anastasia. "Large deformations of nonlinear viscoelastic and multi-responsive beams." International Journal of Non-Linear Mechanics 71 (2015): 152-164.

APPENDIX A

MESH CONVERGENCE STUDY

In finite element (FE) analyses, mesh convergence is conducted in order to determine appropriate element sizes or number and types of elements sufficient to perform the analyses. Mesh convergence determines how many elements are needed to make sure that the result will not change by the element size. In FEM, all structures are divided into a series of discrete points with DOFs (degree of freedom), so the more DOFs there are in the model, the behavior of structures can be captured more precisely. However, more points will increase the computing time. In engineering, there should be a balance between them, which is known as mesh independence study.

For the kerfing patter, the mesh convergence has been conducted on a unit-cell with dense_2 unit section. The load condition is the uniaxial extension and the stroke is 0.2 inch. The element size varied from 0.1 inch to 0.001 inch. The material is MDF (medium density fiberboard) whose elastic modulus is 0.58e6 psi and Poisson's ratio is 0.25.

The results of different element sizes is shown in Table A.1. In order to clearly present the results, Figure A. 1 and Figure A. 2 are shown below to demonstrate the relation of element number and stress and reaction force respectively. According to Figure A. 1 and Figure A. 2, it is illustrated that element size does not affect the result much when element size is 0.003 inch or less, so 0.003 inch is chosen as the element size for the model of dense_2 unit section in all cases.

Table A.1 Results for mesh independence study in dense_2

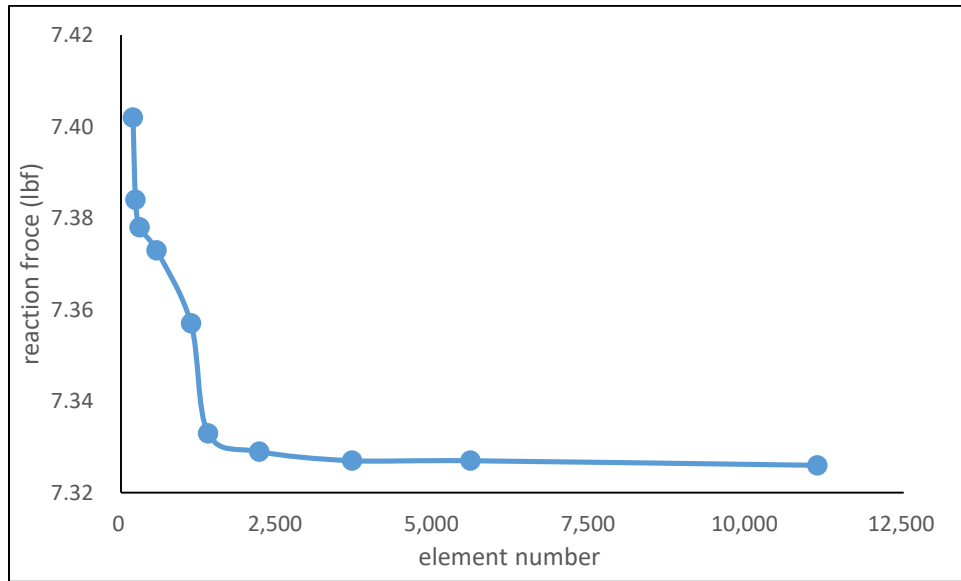| element size/inch	Element number	Stress/psi	reaction force/lbf
0.1	190	8.5250E+03	7.402
0.08	230	8.5410E+03	7.384
0.05	295	8.5650E+03	7.378
0.02	566	8.5910E+03	7.373
0.01	1117	8.6070E+03	7.357
0.008	1391	8.6700E+03	7.333
0.005	2205	8.6720E+03	7.329
0.003	3691	8.6810E+03	7.327
0.002	5579	8.6820E+03	7.327
0.001	11124	8.6840E+03	7.326

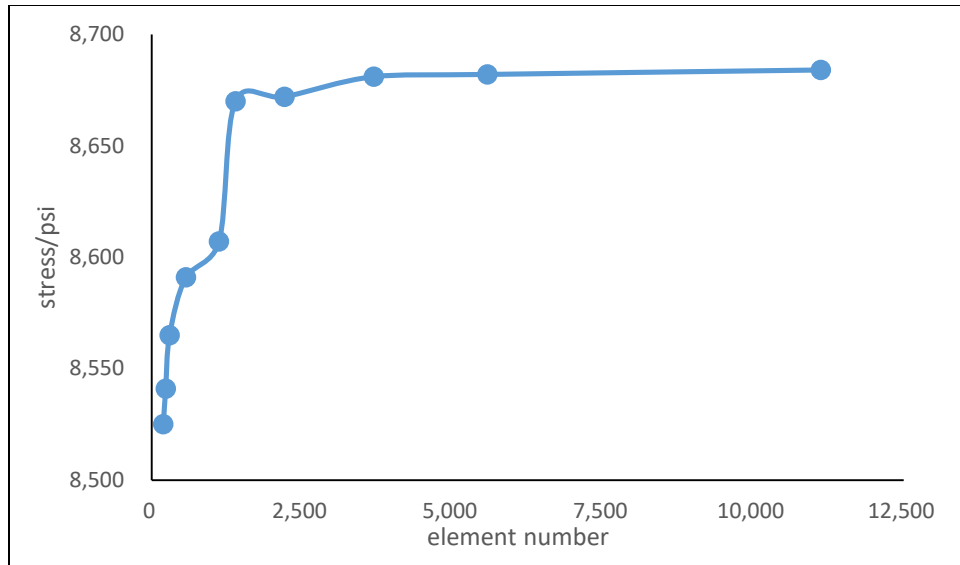**Figure A. 1 The relation of element number and reaction force in dense_2**

Figure A. 2 The relation of element number and stress in dense_2